

Channel Estimation for Reconfigurable Intelligent Surface Assisted High-Mobility Wireless Systems

Chao Xu, *Senior Member, IEEE*, Jiancheng An, Tong Bai, *Member, IEEE*, Shinya Sugiura, *Senior Member, IEEE*, Robert G. Maunder, *Senior Member, IEEE*, Zhaocheng Wang, *Fellow, IEEE*, Lie-Liang Yang, *Fellow, IEEE* and Lajos Hanzo* *Life Fellow, IEEE*

Abstract—Next-generation communication systems aim for providing pervasive services, including the high-mobility scenarios routinely encountered in mission-critical applications. Hence we harness the recently-developed reconfigurable intelligent surfaces (RIS) to assist the high-mobility cell-edge users. More explicitly, the passive elements of RISs generate beneficial phase rotations for the reflected signals, so that the signal power received by the high-mobility users is enhanced. However, in the face of high Doppler frequencies, the existing RIS channel estimation techniques that assume block fading generally result in irreducible error floors. In order to mitigate this problem, we propose a new RIS channel estimation technique, which is the first one that performs minimum mean square error (MMSE) based interpolation for the sake of taking into account the time-varying nature of fading even within the coherence time. The RIS modelling invokes only passive elements without relying on RF chains, where both the direct link and RIS-reflected links as well as both the line-of-sight (LoS) and non-LoS (NLoS) paths are taken into account. As a result, the cascaded base station (BS)-RIS-user links involve the multiplicative concatenation of the channel coefficients in the LoS and NLoS paths across the two segments of the BS-RIS and RIS-user links. Against this background, we model the multiplicative RIS fading correlation functions for the first time in the literature, which facilitates MMSE interpolation for estimating the high-dimensional and high-Doppler RIS-reflected fading channels. Our simulation results demonstrate that for a vehicle travelling at a speed as high as 90 mph, employing a low-complexity RIS at the cell-edge using as few as 16 RIS elements is sufficient for achieving substantial power-efficiency gains, where the Doppler-induced error floor is mitigated by the proposed channel estimation technique.

Index Terms—Reconfigurable intelligent surface, channel estimation, channel state information, minimum mean squared error, high-Doppler, non-line-of-sight, passive beamforming.

I. INTRODUCTION

The recently-developed reconfigurable intelligent surfaces (RIS) [1]–[6] consist of a large number of low-cost passive elements, which are managed by a smart micro controller. Each RIS element is configured to apply an adjustable phase rotation to the signal reflection, so that the received signals

can be constructively enhanced at the desired user and/or destructively nulled at the non-intended users. As a result, RISs are capable of beneficially reconfiguring the wireless propagation environment. More explicitly, first of all, the recent developments in micro-electromechanical systems have enabled the RIS phase shifts to be adjusted near-instantaneously [7], which prevents energy-efficiency loss due to the phase-tuning latency. Secondly, compared to the half-duplex amplify-and-forward (AF) as well as decode-and-forward (DF) relaying schemes [8]–[12], the RIS passively reflects signals without using active radio frequency (RF) chains. As a result, the RIS is capable of operating in full-duplex mode without encountering detrimental self-interference problems. Thirdly, thanks to the elimination of the RF chains, the RIS does not impose extra thermal noise on the reflected signals. Fourthly, since the RIS elements are typically of sub-wavelength size, the low-cost light-weight surface is generally fabricated in a compact form. This facilitates their flexible and low-cost deployment on building facades, room-ceilings, lamp posts, laptop cases or even on human clothing [13], where favourable line-of-sight (LoS) propagation is observed. Furthermore, the integration of RIS in wireless communication systems does not require any standardization modifications. Inspired by these distinct advantages, substantial recent research efforts have been invested in designing smart RIS solutions for a variety of wireless communications scenarios for improving the cellular throughput and coverage-quality [3], [14], [15], the physical layer security [16]–[18], mobile edge computing [19] as well as simultaneous wireless information and power transfer [20].

To reap the appealing benefits of passive RIS in practical systems, it is of paramount importance to obtain accurate Channel State Information (CSI) for phase configuration. However, the CSI acquisition is far from trivial due to both the passive nature of RIS, and due to the associated high-dimensional channels. The existing literature of RIS channel estimation may be classified into the following four main categories. First of all, the LoS-based schemes [14], [21]–[23] configure the RIS purely based on the deterministic LoS knowledge of positioning, angle-of-arrival/departure (AoA/AoD), which lead to sub-optimal solutions due to the fact that the non-LoS (NLoS) propagation components are completely ignored. Secondly, the partially active arrangements of [24]–[26] still rely on a small number of RF chains used for sounding the channels for a certain fraction of the RIS elements. Then the full channel knowledge of all RIS elements may be constructed using compressive sensing and deep learning tools. However, this hybrid philosophy tends to contradict to the motivation of using passive RIS elements, resulting in an increased hardware cost and power consumption. Thirdly, the schemes in [27]–

C. Xu, R. G. Maunder L-L. Yang and L. Hanzo are with the School of Electronics and Computer Science, University of Southampton, Southampton SO17 1BJ, UK (e-mail: {cx1g08,rm,lly,lh}@soton.ac.uk). J. An is with the Engineering Product Development Pillar, Singapore University of Technology and Design, Singapore 487372 (e-mail: jiancheng_an@163.com). Tong Bai is with the School of Cyber Science and Technology, BeihangUniversity, Beijing 100191, China. (e-mail: t.bai@outlook.com). S. Sugiura is with the Institute of Industrial Science, University of Tokyo, Meguro-ku, Tokyo 153-8505, Japan (e-mail: sugiura@ieee.org). Z. Wang is with Tsinghua University, Beijing, China (e-mail: zcwang@tsinghua.edu.cn).

The work of S. Sugiura was supported in part by National Institute of Information and Communications Technology (NICT), Japan. L. Hanzo would like to acknowledge the financial support of the Engineering and Physical Sciences Research Council projects EP/W016605/1 and EP/P003990/1 (CO-ALESCE) as well as of the European Research Council's Advanced Fellow Grant QuantCom (Grant No. 789028).

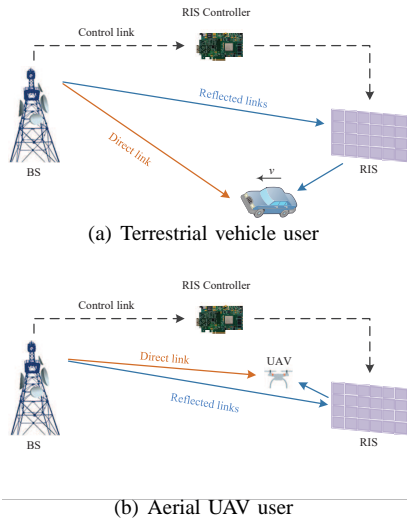


Fig. 1: RIS assisted high-mobility wireless communication systems.

[31] proposed the ON/OFF and discrete Fourier transform (DFT) based RIS patterns for cascaded channel estimation. More explicitly, the ON/OFF based least square (LS) schemes [27], [28] successively estimate the cascaded base station (BS)-RIS-user links by activating a single RIS element in a time slot, so that the interference between RIS elements used for channel estimation is avoided. However, the direct link spanning from the transmitter to the receiver is always present, which constitutes one of the key differences between RISs and the classic backscatter techniques [3]. As a result, the direct link has to be estimated first, which is then subtracted from the subsequent reflected links. In order to improve this, both the LS and the minimum mean squared error (MMSE) methods of [29]–[31] activate all of the RIS elements based on the classic DFT matrix, so that the direct link and all reflected links become orthogonal for channel estimation. Fourthly, as the number of RIS elements grows, the pilot overhead can be further reduced by grouping [27], [32], [33], compressive sensing [34], [35], deep learning [36] and matrix factorization [37]–[40].

At the time of writing, the deployment of 5G New Radio (NR) [41] is well underway. The next-generation wireless communication systems aim for achieving the ambitious goal of 10-fold increased capacity for the enhanced mobile broadband scenarios, in conjunction with ubiquitous coverage. Specifically, high-mobility high-Doppler scenarios are often encountered in the current and future wireless communication networks. To name a few, the 5G systems are envisioned to support a highway car velocity of up to 140 km/h and high-speed train velocity of 500 km/h [42]–[44]. Moreover, the modernization of air traffic management (ATM) plans to improve the existing communication links for aircraft that travel at 1080 km/h [45], [46]. In the much-anticipated space-air-ground integrated network [47], both the 5G networks and the next-generation ATM are developing standards for unmanned aerial vehicles (UAVs) popularly known as drones or quadcopters [48], [49]. The low-altitude rotary-wing UAVs are generally permitted to travel at a speed up to 108 km/h, while the high-altitude fixed-wing UAVs may exceed the speed of sound. For the sake of mitigating the extra costs of capital expenditures (CAPEX) and operating expenses (OPEX) of

building new BSs with short visibility, the RIS is particularly suitable for extending the coverage for the high-mobility terrestrial vehicles or low-altitude UAVs travelling near the cell-edge, as portrayed in Fig. 1.

However, all of the aforementioned RIS designs are based on the idealized simplifying assumption that the fading channels remain constant over the entire frame of signal transmission, as long as the frame duration is within the coherence time. Let us be reminded that the conception of coherence time defines the time duration over which the multipath fading is strongly correlated, rather than being perfectly constant. In the face of high Doppler frequencies, the existing RIS channel estimation techniques that assume perfectly time-invariant block fading generally suffer from irreducible error floors, when *the multipath fading is in fact time-varying albeit correlated within the coherence time*. To elaborate, a selection of representative RIS channel estimation techniques are summarized in Table. I. In terms of RIS modelling, the three essential features of having purely passive elements, taking into account the direct link as well as creating favourable LoS propagation are highlighted in Table. I, where the existing schemes exhibit pros and cons. Furthermore, in the face of high-mobility, the following three key modelling properties are considered in Table. I. **First of all**, the AoAs and AoDs have to be updated in real time. **Secondly**, the LoS path experiences a high frequency offset Δf_{LoS} , which is a function of both the Doppler frequency and of the AoA [44], [50]–[53]. **Thirdly**, the NLoS components become time-varying within coherence time, where the correlation in the time-domain is determined by the normalized maximum Doppler frequency f_d [54], [55]. To the best of our knowledge, the ON/OFF-based MMSE scheme proposed in this paper is the first one that is capable of mitigating the error floor for RIS assisted high-mobility systems operating in time-varying fading channels, as summarized by Table I. In summary, the novel contributions of this work are as follows:

- *New RIS-aided high-mobility system design*: In order to provide reliable coverage for a high-mobility cell-edge user, who may suffer from severe path loss, obstacle-induced blockage and high NLoS attenuation, we propose to deploy a RIS-assisted complementary link. The phase rotations of the reflected links are optimized in order to maximize the received SNR at the high-mobility user. In contrast to the perfectly constant block fading model used in all of the aforementioned RIS-assisted schemes, time-varying Ricean fading channels are considered, where the fading coefficient varies from symbol to symbol. More explicitly, on one hand, both the AoA/AoD as well as the Doppler-induced frequency offset Δf_{LoS} of the LoS component are taken into account. On the other hand, the NLoS components are generated based on Clarke’s model [54], [55], where the correlation between the fading elements versus time is determined by the normalized maximum Doppler frequency f_d .
- *Novel ON/OFF-based MMSE CSI estimation technique*: In the face of high-mobility, the conventional ON/OFF and DFT based channel estimation techniques [27]–[31]

TABLE I: Summary of representative channel estimation techniques for RIS assisted communication systems.

	Scenarios	Method	RIS modelling			Adaptive to mobility		
			Purely passive?	Direct link?	Considered LoS?	Adaptive to AoA/AoD?	Considered Δf_{LoS} ?	Adaptive to high f_d ?
Han <i>et al.</i> [21]	Narrowband single-user	LoS knowledge	✓	✓	✓	✓		
Taha <i>et al.</i> [24]	Wideband single-user	Compressive sensing deep learning				✓		
Yang <i>et al.</i> [27]	Wideband single-user	ON/OFF-based LS	✓	✓	✓			
Wang <i>et al.</i> [28]	Narrowband multi-user	ON/OFF-based LS	✓	✓	✓	✓		
Jensen <i>et al.</i> [29]	Narrowband single-user	DFT-based LS	✓	✓				
Zheng <i>et al.</i> [30]	Wideband single-user	DFT-based LS	✓	✓	✓			
Nadeem <i>et al.</i> [31]	Narrowband multi-user	DFT-based MMSE	✓	✓	✓	✓		
You <i>et al.</i> [33]	Narrowband single-user	DFT-based LS	✓		✓			
Chen <i>et al.</i> [35]	Narrowband multi-user	Compressive sensing	✓			✓		
Ma <i>et al.</i> [36]	Narrowband single-user	Deep learning	✓		✓	✓		
He <i>et al.</i> [37]	Narrowband single-user	Matrix factorization	✓			✓		
Liu <i>et al.</i> [40]	Narrowband multi-user	Matrix factorization	✓	✓	✓	✓		
Our solution	Narrowband single-user	ON/OFF-based MMSE	✓	✓	✓	✓	✓	✓

all inevitably suffer from irreducible error floors. In order to mitigate this problem, we propose a novel ON/OFF-based MMSE channel estimation scheme for RIS-aided high-mobility systems. Taking into account the distinct RIS properties, we suitably adapt the conventional channel estimation techniques for the direct-link-only scenario [44], [48], [50]–[52] in the following three major aspects. **Firstly**, the proposed ON/OFF-based MMSE technique requires a total number of $(1 + M)$ time slots for evaluating the direct link and the M reflected links one by one, where the estimated direct link has to be subtracted from the estimates of the reflected links. **Secondly**, the conventional direct-link-only communication techniques [44], [48], [50]–[52] are generally assumed to be able to buffer a large number of frames. Explicitly, when evaluating the CSI of the u -th frame, the conventional techniques take into account both $\lfloor N_w/2 \rfloor$ pilots from the “past” frames transmitted before the u -th frame as well as $(N_w - \lfloor N_w/2 \rfloor - 1)$ pilots from the “future” frames transmitted after the u -th frame. By contrast, in the RIS-assisted systems, the proposed technique has to provide instantaneous CSI estimation for the sake of RIS phase configuration, hence only the frames received in the past can be exploited. **Thirdly**, the fading model of the RIS-assisted high-mobility systems has to adapt to both the improved dimension and the RIS-induced multiplicative fading correlation functions, where the cascaded BS-RIS-user links involve multiplications of the LoS and NLoS elements across the two segments of BS-RIS and RIS-user links. Against this background, we model the multiplicative RIS fading correlation functions for the first time in the literature, which facilitates MMSE interpolation for estimating the high-dimensional high-Doppler RIS-reflected fading channels.

- **Numerical validations and evaluations:** Both analytical and numerical results are provided for the sake of validating the performance of our RIS assisted high-mobility wireless systems. Our simulation results demonstrate that for a vehicle travelling at a speed as high as 90 mph, employing a low-complexity RIS at the cell-edge using as few as 16 RIS elements is sufficient for achieving substantial power-efficiency improvements, where the Doppler-induced error floor is mitigated by the proposed channel estimation technique.

The rest of this paper is organized as follows. Our RIS-assisted high-mobility system model and our problem formu-

lation are discussed in Sec. II. The existing channel estimation techniques and the proposed solutions are presented in Sec. III. Finally, our system performance results and conclusions are offered in Sec. IV and Sec. V, respectively.

The following notations are used throughout the paper. The operations $(\cdot)^*$ and $(\cdot)^H$ denote the conjugate of a complex number and the Hermitian transpose of a complex matrix, respectively. $\ln(\cdot)$ and $\exp(\cdot)$ refer to natural logarithm and natural exponential functions, respectively. $p(\cdot)$ and $E(\cdot)$ represent the probability and the expectation, respectively. $\mathcal{CN}(\mu, \sigma^2)$ refers to complex Gaussian distribution with mean μ and variance σ^2 . $\mathbf{a} \in \mathcal{C}^{N \times 1}$ refers to a complex-valued vector of size $(N \times 1)$, and $\mathbf{A} \in \mathcal{C}^{c \times d}$ denotes that \mathbf{A} is a complex-valued matrix of size $(c \times d)$.

II. SYSTEM MODELLING AND PROBLEM FORMULATION

A. Three-Dimensional Schematic Representation

We consider a downlink scenario where the coverage of a high-mobility user is enhanced by a RIS, as portrayed in Fig. 1. In this paper, a single antenna is used both at the source and at the destination, which minimizes the CSI estimation overhead in the high-mobility scenarios considered. We note that as the number of antennas is increased at the BS and/or the user, the channel estimation scheme conceived in this paper can be directly applied using an ON/OFF pattern of antennas. However, this results in both an excessive pilot overhead and an extended interpolation window for the high-dimensional RIS link that grows with the number of antennas, which is not preferred in the high-mobility scenarios considered in this paper.

The RIS is assumed to be comprised of M passive reflecting elements, where a uniform planar array (UPA) is adopted. The RIS phase rotations at the n -th time slot are configured as $\boldsymbol{\alpha}_n = [\alpha_n^1, \dots, \alpha_n^M]^T$, where $\{|\alpha_n^m| = 1\}_{m=1}^M$ are optimized by maximizing the received signal power at the destination. Moreover, the destination is emerging from the cell-edge travelling at a velocity v , where the moving direction is not necessarily directly towards the BS. The direct link suffers from severe path loss, blockage and high NLoS attenuation. The RIS-assisted reflected links are assumed to be able to create a favourable propagation environment.

The block fading assumed in the existing solutions of Table I are no longer valid in high-mobility situations. Consider a system having 100 kHz of bandwidth centered at $f_c = 2.6$ GHz in the S-band [48], which is sufficient for high-mobility Command & Control (C&C) link coverage [45]. If the user

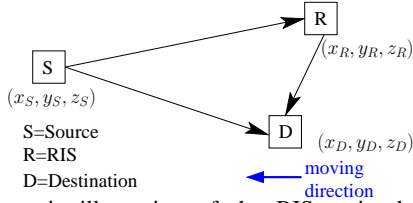


Fig. 2: Schematic illustration of the RIS assisted high-mobility wireless communication system.

moves at 90 mph, the coherence time over which the time correlation function is higher than 0.5 is estimated to cover only 51 symbols, which significantly differs from the idealistic assumption, namely that channel remains 100% constant over an entire frame of signal transmission. In this treatise, we stipulate the challenging time-varying assumption that the coherence time is limited to a single symbol duration [56]–[59], i.e. the Ricean fading components are different for each symbol index n , where the correlation function across different symbols in the time-domain is determined by the Doppler frequency based on the Clarke’s model [54], [55]. The three-dimensional (3D) coordinates seen in Fig. 2 are used for instantaneously updating the path loss (PL) and the deterministic LoS components in Ricean fading. The RIS-reflected signals are time-delayed by $\frac{\alpha_n^m}{2\pi f_c} \leq \frac{1}{f_c}$, which is negligible compared to the symbol period $\frac{1}{f_s}$ when $f_s \ll f_c$ is satisfied. Moreover, the time-varying Ricean fading channels investigated in this paper are assumed to be flat, which is reasonable for a C&C link of $f_s = 100$ kHz over a coverage distance on the order of hundreds of meters.

B. Source-Destination Link

The PL of the direct source-destination (SD) link in Fig. 2 is expressed as:

$$\text{PL}(d^{SD}) = -10\gamma^{SD} \log_{10} \frac{d^{SD}}{d_0} - \text{PL}_0 = 10 \log_{10} \Gamma^{SD} \text{ dB}, \quad (1)$$

where γ^{SD} denotes the PL exponent of the SD link, while PL_0 is the path loss at the reference distance of $d_0 = 1$ m. The distance is evaluated by $d^{SD} = \sqrt{(x_S - x_D)^2 + (y_S - y_D)^2 + (z_S - z_D)^2}$. The non-logarithmic PL of the SD link is given by $\Gamma^{SD} = 10^{0.1\text{PL}}$. The high-mobility small-scale Ricean fading is comprised of both LoS and NLoS components: [44], [50]–[53]

$$h_n^{SD} = h_n^{\text{SD-LoS}} + h_n^{\text{SD-NLoS}} = \sqrt{\frac{\Gamma_n^{\text{SD}} K^{\text{SD}}}{1+K^{\text{SD}}}} \exp(j2\pi n \Delta f_n^{\text{SD-LoS}}) + h_n^{\text{SD-NLoS}} \quad (2)$$

The time index $n \in \mathcal{N}$ is positive integer. Both LoS and NLoS components of (2) vary for each symbol index n , where the time-varying nature is determined by the Doppler frequencies. More explicitly, the LoS component of (2) is given by $h_n^{\text{SD-LoS}} = \sqrt{\frac{\Gamma_n^{\text{SD}} K^{\text{SD}}}{1+K^{\text{SD}}}} \exp(j2\pi n \Delta f_n^{\text{SD-LoS}})$, where the Ricean K-factor determines the power ratio between the LoS and the NLoS components. The frequency offset of the LoS path is induced by the movement of the destination:

$$\Delta f_n^{\text{SD-LoS}} = f_d^{\text{SD}} \cos(\phi_0^{\text{SD}}). \quad (3)$$

The normalized maximum Doppler frequency of the SD link is given by $f_d^{\text{SD}} = \frac{v f_c}{c f_s}$, where v , f_c , c , f_s represent the destination’s velocity, the carrier frequency, the speed of light and the

symbol rate, respectively. The angle between the LOS and the moving direction in (3) is evaluated by $\phi_0^{\text{SD}} = \arctan \frac{y_S - y_D}{x_S - x_D}$. We note that both the path loss Γ_n^{SD} and the AoA ϕ_0^{SD} from (1) to (3) are time-varying based on the coordinates (x_S, y_S, z_S) and (x_D, y_D, z_D) . Moreover, the NLoS component in (2) is generated by Clarke’s model [54], [55] associated with a power of $\frac{\Gamma_n^{\text{SD}}}{1+K^{\text{SD}}}$ as $h_n^{\text{SD-NLoS}} \sim \mathcal{CN}(0, \frac{\Gamma_n^{\text{SD}}}{1+K^{\text{SD}}})$. The correlation over time is given by $E[h_{n'}^{\text{SD-NLoS}}(h_n^{\text{SD-NLoS}})^*] = \frac{\sqrt{\Gamma_n^{\text{SD}} \Gamma_{n'}^{\text{SD}}}}{1+K^{\text{SD}}} J_0(2\pi f_d^{\text{SD}} |n - n'|)$, where $J_0(\cdot)$ is the Bessel function of the first kind.

C. Source-RIS Links

For the source-RIS (SR) links, the PL is evaluated in the same way as in (1), where γ^{SD} , d^{SD} and Γ^{SD} are replaced by γ^{SR} , d^{SR} and Γ^{SR} based on the coordinates (x_S, y_S, z_S) and (x_R, y_R, z_R) . The M -element Ricean fading vector of the SR links is given by: [44], [50]–[53]

$$\mathbf{h}_n^{\text{SR}} = \mathbf{h}_n^{\text{SR-LoS}} + \mathbf{h}_n^{\text{SR-NLoS}}. \quad (4)$$

The M -element LoS paths $\mathbf{h}_n^{\text{SR-LoS}} \in \mathbb{C}^{M \times 1}$ are formulated as:

$$\mathbf{h}_n^{\text{SR-LoS}} = \sqrt{\frac{\Gamma_n^{\text{SR}} K^{\text{SR}}}{1+K^{\text{SR}}}} \exp(j2\pi n \Delta f_n^{\text{SR-LoS}}) \mathbf{a}_r(\theta^r, \varphi^r), \quad (5)$$

where the azimuth and elevation AoAs are evaluated based on the 3-D coordinates as $\theta^r = \arccos \frac{z_S - z_R}{d^{\text{SR}}}$ and $\varphi^r = \arctan \frac{y_S - y_R}{x_S - x_R}$. For the UPA having M_y and M_z elements on the y and z axes, the array response vector is given by:

$$\mathbf{a}_{\text{UPA}}(\theta, \varphi) = [1, \dots, \exp\{j \frac{2\pi}{\lambda} d [m_y \sin \theta \cos \varphi + m_z \sin \varphi]\}, \dots, \exp\{j \frac{2\pi}{\lambda} d [(M_y - 1) \sin \theta \cos \varphi + (M_z - 1) \sin \varphi]\}]^T, \quad (6)$$

where we have $[1 \leq m_y \leq (M_y - 1)]$, $[1 \leq m_z \leq (M_z - 1)]$ and $M = M_y M_z$, while $\lambda = \frac{c}{f_c}$ and $d = \frac{\lambda}{2}$ denote the wavelength and antenna spacing, respectively. The LoS offset $\Delta f_n^{\text{SR-LoS}}$ of (5) is evaluated in the same way as (3), where the destination coordinate (x_D, y_D, z_D) is replaced by the RIS coordinate (x_R, y_R, z_R) . Moreover, each element in the NLoS vector of $\mathbf{h}_n^{\text{SR-NLoS}} \in \mathbb{C}^{M \times 1}$ in (4) is independently generated by Clarke’s model as $h_n^{\text{SR-NLoS}m} = [h_n^{\text{SR-NLoS}}]_m \sim \mathcal{CN}(0, \frac{\Gamma_n^{\text{SR}}}{1+K^{\text{SR}}})$, where the correlation is given by $E[h_{n'}^{\text{SR-NLoS}m}(h_n^{\text{SR-NLoS}m})^*] = \frac{\sqrt{\Gamma_n^{\text{SR}} \Gamma_{n'}^{\text{SR}}}}{1+K^{\text{SR}}} J_0(2\pi f_d^{\text{SR}} |n - n'|)$.

We note that the implementation of RIS with high-precision discrete-phase is envisioned to have smaller size of $d < \frac{\lambda}{2}$ [60], which leads to spatial correction [61]. To elaborate, on one hand, the smaller RIS elements suffer from coupling issues and are more expensive to build. On the other hand, the relatively large RIS elements leads to higher quantization errors. We opt for assuming $d = \frac{\lambda}{2}$ in RIS modelling first, and then we will demonstrate in Sec. IV that coarse RIS quantization does not inflict significant impairments in the high-mobility scenarios considered. Nonetheless, we note that the spatial correlation imposed by $d < \frac{\lambda}{2}$ will not affect the channel estimation method proposed in this treatise, which operates based on the time-domain correlation of each RIS element, regardless of their spatial-domain correlation.

D. RIS-Destination Links

For the RIS-destination (RD) links, the PL of (1) is evaluated based on (x_R, y_R, z_R) and (x_D, y_D, z_D) , where γ^{SD} , d^{SD} and Γ^{SD} in (1) are replaced by γ^{RD} , d^{RD} and Γ^{RD} . The M -element small-scale Ricean fading row-vector of the RD links is given by:

$$\mathbf{h}_n^{\text{RD}} = \mathbf{h}_n^{\text{RD-LoS}} + \mathbf{h}_n^{\text{RD-NLoS}}. \quad (7)$$

The M -element LoS row-vector $\mathbf{h}_n^{\text{RD-LoS}} \in \mathbb{C}^{1 \times M}$ is formulated as:

$$\mathbf{h}_n^{\text{RD-LoS}} = \sqrt{\frac{\Gamma_n^{\text{RD}} K^{\text{RD}}}{1+K^{\text{RD}}}} \exp(j2\pi n \Delta f_n^{\text{RD-LoS}}) \mathbf{a}_t(\theta^t, \varphi^t)^H, \quad (8)$$

where the UPA response vector is given by (6). The azimuth and elevation AoDs are evaluated as $\theta^t = \arccos \frac{z_D - z_R}{d^{\text{RD}}}$ and $\varphi^t = \arctan \frac{y_D - y_R}{x_D - x_R}$, respectively. The LoS frequency offset of (8) is $\Delta f_n^{\text{RD-LoS}} = f_d^{\text{RD}} \cos(\phi_0^{\text{RD}})$, where the angle between the LOS and the moving direction is evaluated by $\phi_0^{\text{RD}} = \arctan \frac{y_R - y_D}{x_R - x_D}$. Moreover, each element in the NLoS row-vector of $\mathbf{h}_n^{\text{RD-NLoS}} \in \mathbb{C}^{1 \times M}$ is independently generated by Clarke's model as $h_n^{\text{RD-NLoS}m} = [\mathbf{h}_n^{\text{RD-NLoS}}]_m \sim \mathcal{CN}(0, \frac{\Gamma_n^{\text{RD}}}{1+K^{\text{RD}}})$, where the correlation is $E[h_n^{\text{RD-NLoS}m} (h_{n'}^{\text{RD-NLoS}m})^*] = \frac{\sqrt{\Gamma_n^{\text{RD}} \Gamma_{n'}^{\text{RD}}}}{1+K^{\text{RD}}} J_0(2\pi f_d^{\text{RD}} |n - n'|)$. Since the RIS is implemented by a dense population of repeated meta-atoms, where the size of meta-atom is typically on the order of the subwavelength of the operating frequency [6], the RIS elements are assumed to share the same maximum Doppler frequency, which is the same as the assumption for the co-located multiple antennas in high-mobility scenarios [44], [59].

E. Received Signal Modelling

In the absence of active RF chains, the RIS does not impose signal processing latency. As a result, the signals of both the direct link and of the reflected links arrive at the destination within the same symbol-level sampling period, as discussed in Sec. II-A, yielding:

$$\begin{aligned} y_n &= [h_n^{\text{SD}} + \mathbf{h}_n^{\text{RD}} \text{diag}(\boldsymbol{\alpha}_n) \mathbf{h}_n^{\text{SR}}] s_n + v_n \\ &= [h_n^{\text{SD}} + \sum_{m=1}^M \alpha_n^m h_n^{\text{SRD}m}] s_n + v_n, \end{aligned} \quad (9)$$

where the cascaded RIS-reflected links are represented by $h_n^{\text{SRD}m} = [\mathbf{h}_n^{\text{SRD}}]_m = [\mathbf{h}_n^{\text{SR}}]_m [\mathbf{h}_n^{\text{RD}}]_m$ and we have $\mathbf{h}_n^{\text{SRD}} \in \mathbb{C}^{M \times 1}$. Moreover, $v_n \sim \mathcal{CN}(0, N_0)$ is the receiver's additive white Gaussian noise (AWGN) associated with power N_0 .

For the sake of channel estimation, let us arrange the signal transmission in frames. The n -th symbol in (9) may be regarded as the t -th symbol in the u -th frame expressed as $n = uN_f + t$, where N_f denotes the frame length. For the sake of accurate channel estimation, the first $(1+M)$ symbols in each frame are pilots known to both the transmitter and receiver, while the remaining $[N_f - (1+M)]$ symbols carry source information. The pilot percentage is therefore given by $\eta_p = \frac{(M+1)}{N_f}$. This implies that a smaller N_f leads to a smaller pilot spacing and a higher pilot percentage, hence an improved CSI estimation accuracy. However, it is worth noting that a higher pilot percentage also results in an effective throughput loss, which inevitably imposes an estimation accuracy versus

throughput tradeoff. In summary, the received signals of (9) can be modelled in the following form:

$$\begin{aligned} y_{u,t} &= [h_{u,t}^{\text{SD}} + (\mathbf{h}_{u,t}^{\text{SRD}})^T \boldsymbol{\alpha}_{u,t}] s_{u,t} + v_{u,t} \\ &= \mathbf{h}_{u,t} \bar{\boldsymbol{\alpha}}_{u,t} s_{u,t} + v_{u,t} = h_{u,t}^{\text{RIS}} s_{u,t} + v_{u,t}, \end{aligned} \quad (10)$$

for $t = 1, \dots, N_f$, where we have $n = uN_f + t$, $\mathbf{h}_{u,t} = [h_{u,t}^{\text{SD}}, (\mathbf{h}_{u,t}^{\text{SRD}})^T] \in \mathbb{C}^{1 \times (M+1)}$ and $\bar{\boldsymbol{\alpha}}_{u,t}^p = [1, \boldsymbol{\alpha}_{u,t}^T]^T \in \mathbb{C}^{(M+1) \times 1}$. The pilot symbols and the data-bearing symbols are associated with $t = 1, \dots, 1+M$ and $t = 2+M, \dots, N_f$, respectively. The equivalent fading element in (10) is given by $h_{u,t}^{\text{RIS}} = [h_{u,t}^{\text{SD}} + (\mathbf{h}_{u,t}^{\text{SRD}})^T \boldsymbol{\alpha}_{u,t}] = \mathbf{h}_{u,t} \bar{\boldsymbol{\alpha}}_{u,t}$. The objective of the RIS phase configuration is to maximize the SNR of (10), subject to the constant-envelope constraints of $\{|\alpha_{u,t}^m| = 1\}_{m=1}^M$ [3], [62], which will be further elaborated on in the next section.

F. Problem Formulation

Let us first consider the following Lemma 1 for maximizing the ergodic capacity.

Lemma 1: For the RIS-assisted system model of (10), we assume that the ergodic fading processes of $\{h_{u,t}^{\text{SD}}\}_{u,t \in \mathcal{N}}$, $\{\{h_{u,t}^{\text{SR}m}\}_{u,t \in \mathcal{N}}\}_{m=1}^M$ and $\{\{h_{u,t}^{\text{RD}m}\}_{u,t \in \mathcal{N}}\}_{m=1}^M$ as well as the ergodic noise process of $\{v_{u,t}\}_{u,t \in \mathcal{N}}$ are independent of each other. Then the ergodic capacity that maximizes the mutual information $I(s_{u,t}; y_{u,t})$ between the random variables of channel input $s_{u,t}$ and output $y_{u,t}$ is given by:

$$R_I = \max_{\alpha_{u,t}^m} E \left[\log_2 \left(1 + \frac{|h_{u,t}^{\text{SD}} + \sum_{m=1}^M \alpha_{u,t}^m h_{u,t}^{\text{SRD}m}|^2}{N_0} \right) \right], \quad (11a)$$

$$= E \left\{ \log_2 \left[1 + \frac{|h_{u,t}^{\text{SD}}|^2 \left(1 + \frac{\sum_{m=1}^M |h_{u,t}^{\text{SRD}m}|}{|h_{u,t}^{\text{SD}}|} \right)^2}{N_0} \right] \right\}, \quad (11b)$$

when the perfect CSIs of $h_{u,t}^{\text{SD}}$, $h_{u,t}^{\text{SR}m}$ and $h_{u,t}^{\text{RD}m}$ are known at the receiver only.

Proof. See Appendix A. \square

Taking this one step further, since the overall fading process $h_{u,t}^{\text{RIS}}$ is Gaussian-distributed for large M , the mean and variance of its Ricean-distributed amplitude $|h_{u,t}^{\text{RIS}}|$ associated with the optimized RIS configuration may be further evaluated as follows. $|h_{u,t}^{\text{SR}m}|$ is Ricean distributed with the mean of $\frac{\sqrt{\pi \Gamma^{\text{SR}}}}{2} \mathcal{L}_{\frac{1}{2}}(-K^{\text{SR}})$ and the variance of $\Gamma^{\text{SR}} - \frac{\pi \Gamma^{\text{SR}}}{4} \mathcal{L}_{\frac{1}{2}}^2(-K^{\text{SR}})$, where $\mathcal{L}_{\frac{1}{2}}(x)$ denotes the Laguerre polynomial of degree 1/2. Similarly, $|h_{u,t}^{\text{RD}m}|$ is also Ricean distributed with the mean of $\frac{\sqrt{\pi \Gamma^{\text{RD}}}}{2} \mathcal{L}_{\frac{1}{2}}(-K^{\text{RD}})$ and the variance of $\Gamma^{\text{RD}} - \frac{\pi \Gamma^{\text{RD}}}{4} \mathcal{L}_{\frac{1}{2}}^2(-K^{\text{RD}})$. As a result, the mean and variance of $|h_{u,t}^{\text{SRD}m}|$ are $\frac{\pi}{4} \sqrt{\Gamma^{\text{SR}} \Gamma^{\text{RD}}} \mathcal{L}_{\frac{1}{2}}(-K^{\text{SR}}) \mathcal{L}_{\frac{1}{2}}(-K^{\text{RD}})$ and $\left[\Gamma^{\text{SR}} \Gamma^{\text{RD}} - \frac{\pi}{4} \Gamma^{\text{SR}} \Gamma^{\text{RD}} \mathcal{L}_{\frac{1}{2}}^2(-K^{\text{SR}}) \mathcal{L}_{\frac{1}{2}}^2(-K^{\text{RD}}) \right]$, respectively. Therefore, the amplitude of the overall fading process associated with the optimized RIS configuration $|h_{u,t}^{\text{RIS}}| =$

$|h_{u,t}^{\text{SD}}| + \sum_{m=1}^M |h_{u,t}^{\text{SRD}m}|$ in (11b) has the following mean and variance:

$$\begin{aligned} \mu &= \frac{\sqrt{\pi}\Gamma^{\text{SD}}}{2} \mathcal{L}_{\frac{1}{2}}(-K^{\text{SD}}) + \frac{M\pi}{4} \sqrt{\Gamma^{\text{SR}}\Gamma^{\text{RD}}} \mathcal{L}_{\frac{1}{2}}(-K^{\text{SR}}) \mathcal{L}_{\frac{1}{2}}(-K^{\text{RD}}), \\ \sigma^2 &= \Gamma^{\text{SD}} - \frac{\pi\Gamma^{\text{SD}}}{4} \mathcal{L}_{\frac{1}{2}}^2(-K^{\text{SD}}) + \\ &M \left[\Gamma^{\text{SR}}\Gamma^{\text{RD}} - \frac{\pi}{4} \Gamma^{\text{SR}}\Gamma^{\text{RD}} \mathcal{L}_{\frac{1}{2}}^2(-K^{\text{SR}}) \mathcal{L}_{\frac{1}{2}}^2(-K^{\text{RD}}) \right]. \end{aligned} \quad (12)$$

However, in the presence of realistic CSI estimation errors, the ergodic capacity of Lemma 1 cannot be achieved. We will conceive an MMSE estimation method in Sec. III, where the direct link and the RIS-reflected links are estimated one by one. The associated achievable rate is investigated by the following Proposition 1.

Proposition 1: Assume that the direct link $h_{u,t}^{\text{SD}}$ and the RIS-reflected links $\{h_{u,t}^{\text{SRD}m}\}_{m=1}^M$ are separately estimated by the MMSE method, yielding the estimated CSI of $\hat{h}_{u,t}^{\text{SD}}$ and $\{\hat{h}_{u,t}^{\text{SRD}m}\}_{m=1}^M$, where the CSI estimation errors are denoted by $\Delta h_{u,t}^{\text{SD}} = \hat{h}_{u,t}^{\text{SD}} - h_{u,t}^{\text{SD}}$ and $\{\Delta h_{u,t}^{\text{SRD}m} = \hat{h}_{u,t}^{\text{SRD}m} - h_{u,t}^{\text{SRD}m}\}_{m=1}^M$. Given the same assumptions concerning the fading processes and Gaussian input distribution as Lemma 1, the achievable rate based on the estimated CSI is given by:

$$R_{II} = (1 - \eta_p) E \left[\log_2 \left(1 + \frac{|\hat{h}_{u,t}^{\text{SD}} + \sum_{m=1}^M \hat{\alpha}_{u,t}^m \hat{h}_{u,t}^{\text{SRD}m}|^2}{N_0 + \sigma_{\text{MSE}}^2} \right) \right], \quad (13a)$$

$$= (1 - \eta_p) E \left\{ \log_2 \left[1 + \frac{|\hat{h}_{u,t}^{\text{SD}}|^2 \left(1 + \frac{\sum_{m=1}^M |\hat{h}_{u,t}^{\text{SRD}m}|^2}{|\hat{h}_{u,t}^{\text{SD}}|^2} \right)}{N_0 + \sigma_{\text{MSE}}^2} \right] \right\}, \quad (13b)$$

where the RIS can only be configured by the realistically estimated CSI as $\hat{\alpha}_{u,t}^m = \frac{\hat{h}_{u,t}^{\text{SD}} (\hat{h}_{u,t}^{\text{SRD}m})^*}{|\hat{h}_{u,t}^{\text{SD}} \hat{h}_{u,t}^{\text{SRD}m}|}$, while the pilot percentage η_p is also taken into account. The MSE is given by $\sigma_{\text{MSE}}^2 = E(\|h_{u,t}^{\text{RIS}} - \hat{h}_{u,t}^{\text{RIS}}\|^2)$, where $\hat{h}_{u,t}^{\text{RIS}}$ refers to the MMSE estimate of $h_{u,t}^{\text{RIS}} = h_{u,t}^{\text{SD}} + \sum_{m=1}^M \alpha_{u,t}^m h_{u,t}^{\text{SRD}m}$.

Proof. See Appendix B. \square

The ergodic capacity of Lemma 1 and the achievable rate of Proposition 1 are derived based on the Gaussian input distribution for the random variable $s_{u,t}$. However, when a specific LPSK/QAM constellation is considered, the achievable rate of a discrete memoryless channel [58], [63]–[65] is characterized by the following Lemma 2.

Lemma 2: When the Gaussian input distribution of Lemma 1 is replaced by a specific LPSK/QAM input constellation with equiprobable occurrence, the achievable rate becomes (14), where we have $\text{BPS} = \log_2 L$ and $\{p(s^l) = \frac{1}{L}\}_{l=1}^L$ for a fixed L .

Proof. (14a) is defined by [63, (3)] associated with $\{p(s^l) = \frac{1}{L}\}_{l=1}^L$, and it can be extended as:

$$\begin{aligned} R_{III} &= E \left[\log_2 \frac{L p(y|s^l)}{\sum_{l'=1}^L p(y|s^{l'})} |s^l \right] \\ &= \text{BPS} - \frac{1}{L} \sum_{l=1}^L E \left\{ \log_2 \left[\sum_{l'=1}^L \frac{p(y|s^{l'})}{p(y|s^l)} |s^l \right] \right\}. \end{aligned} \quad (16)$$

TABLE II: Summary of achievable rate analysis.

Achievable rates	Input	Side information	Configuring RIS
R_I (Lemma 1)	Gaussian	Perfect CSI	Perfect CSI
R_{II} (Proposition 1)	Gaussian	Estimated CSI	Estimated CSI
R_{III} (Lemma 2)	LPSK/QAM	Perfect CSI	Perfect CSI
R_{IV} (Proposition 2)	LPSK/QAM	Estimated CSI	Estimated CSI

Since the expectation is conditioned on s^l , the conditional probabilities based on (10) are given by $p(y|s^l) = \frac{1}{\pi N_0} \exp(-\frac{|y_{u,t} - h_{u,t}^{\text{RIS}} s^l|^2}{N_0}) = \frac{1}{\pi N_0} \exp(-\frac{|v_{u,t}|^2}{N_0})$ and $p(y|s^{l'}) = \frac{1}{\pi N_0} \exp(-\frac{|y_{u,t} - h_{u,t}^{\text{RIS}} s^{l'}|^2}{N_0}) = \frac{1}{\pi N_0} \exp(-\frac{|h_{u,t}^{\text{RIS}}(s^l - s^{l'}) + v_{u,t}|^2}{N_0})$, where the received signal is given by $y_{u,t} = h_{u,t}^{\text{RIS}} s^l + v_{u,t}$. Following this, (14b) can be obtained from (16) by using these conditional probabilities. \square

Finally, in the presence of CSI estimation errors, the achievable rate of Lemma 2 becomes the following Proposition 2.

Proposition 2: When relying on the CSI estimate $\hat{h}_{u,t}^{\text{RIS}}$, the achievable rate of (14) becomes (15).

Proof. In the presence of CSI estimation errors, the conditional probabilities of (15a) become

$$\begin{aligned} p(y|s^l, \hat{h}) &= \frac{1}{\pi(N_0 + \sigma_{\text{MSE}}^2)} \exp(-\frac{|y_{u,t} - \hat{h}_{u,t}^{\text{RIS}} s^l|^2}{(N_0 + \sigma_{\text{MSE}}^2)}) = \\ &\frac{1}{\pi(N_0 + \sigma_{\text{MSE}}^2)} \exp(-\frac{|\Delta h_{u,t}^{\text{RIS}} s^l + v_{u,t}|^2}{(N_0 + \sigma_{\text{MSE}}^2)}) \quad \text{and} \\ p(y|s^{l'}, \hat{h}) &= \frac{1}{\pi(N_0 + \sigma_{\text{MSE}}^2)} \exp(-\frac{|y_{u,t} - \hat{h}_{u,t}^{\text{RIS}} s^{l'}|^2}{(N_0 + \sigma_{\text{MSE}}^2)}) = \\ &\frac{1}{\pi(N_0 + \sigma_{\text{MSE}}^2)} \exp(-\frac{|h_{u,t}^{\text{RIS}} s^l - \hat{h}_{u,t}^{\text{RIS}} s^{l'} + v_{u,t}|^2}{(N_0 + \sigma_{\text{MSE}}^2)}), \text{ leading to (15b). } \quad \square \end{aligned}$$

Finally, the achievable rates of this section are summarized in Table II, which will be invoked for examining the performance of the proposed RIS channel estimation method in Sec. IV-A.

III. CHANNEL ESTIMATION TECHNIQUES

The schematics of channel estimation techniques are compared in Fig. 3. For the conventional direct-link-only techniques [44], [48], [50]–[52] of Fig. 3(a), the receiver is assumed to be capable of receiving and buffering a large number of frames. Specifically, when performing CSI acquisition for the u -th frame, the direct-link-only MMSE-based technique of Fig. 3(a) takes into account all the $\lfloor N_w/2 \rfloor$ pilots from the “past” frames transmitted before the u -th frame, as well as the single pilot of the current u -th frame and also the $(N_w - \lfloor N_w/2 \rfloor - 1)$ pilots from the “future” frames transmitted after the u -th frame. By contrast, the proposed RIS technique of Fig. 3(c) has to provide instantaneous CSI estimation for the sake of RIS phase configuration, hence only the pilots from the past $(N_w - 1)$ frames and the current u -th frame can be utilized, where each frame has $(M + 1)$ pilot symbols for estimating the direct and RIS-reflected links. The ON/OFF and DFT based LS technique of Fig. 3(b) operates based on the assumption that the fading channels remain constant over the entire frame of signal transmission, hence channel estimation is performed purely based on the $(M + 1)$ pilots transmitted at the beginning of the current u -th frame. By contrast, the proposed MMSE-based RIS technique of Fig. 3(c) performs channel estimation based on both the pilots from the past $(N_w - 1)$ frames as well as the pilots of the current u -th frame. Moreover, we note that for the RIS techniques of Fig. 3(b) and Fig. 3(c), upon obtaining the estimated CSI of the u -th frame, a short interval is required for RIS configuration before

$$R_{III} = \sum_{l=1}^L \int p(y|s^l)p(s^l) \log_2 \frac{p(y|s^l)}{\sum_{l'=1}^L p(y|s^{l'})p(s^{l'})} dy \quad (14a)$$

$$= \text{BPS} - \frac{1}{L} \sum_{l=1}^L E \left\{ \log_2 \left[\sum_{l'=1}^L \exp \left(\frac{-|h_{u,t}^{\text{RIS}}(s^l - s^{l'}) + v_{u,t}|^2 + |v_{u,t}|^2}{N_0} \right) \right] \right\}, \quad (14b)$$

$$R_{IV} = E \left[\log_2 \frac{L p(y|s^l, \hat{h})}{\sum_{l'=1}^L p(y|s^{l'}, \hat{h})} |s^l \right] \quad (15a)$$

$$= (1 - \eta_p) \text{BPS} - \frac{(1 - \eta_p)}{L} \sum_{l=1}^L E \left\{ \log_2 \left[\sum_{l'=1}^L \exp \left(\frac{-|h_{u,t}^{\text{RIS}} s^l - \hat{h}_{u,t}^{\text{RIS}} s^{l'} + v_{u,t}|^2 + |\Delta h_{u,t}^{\text{RIS}} s^l + v_{u,t}|^2}{N_0 + \sigma_{\text{MSE}}^2} \right) \right] \right\}. \quad (15b)$$

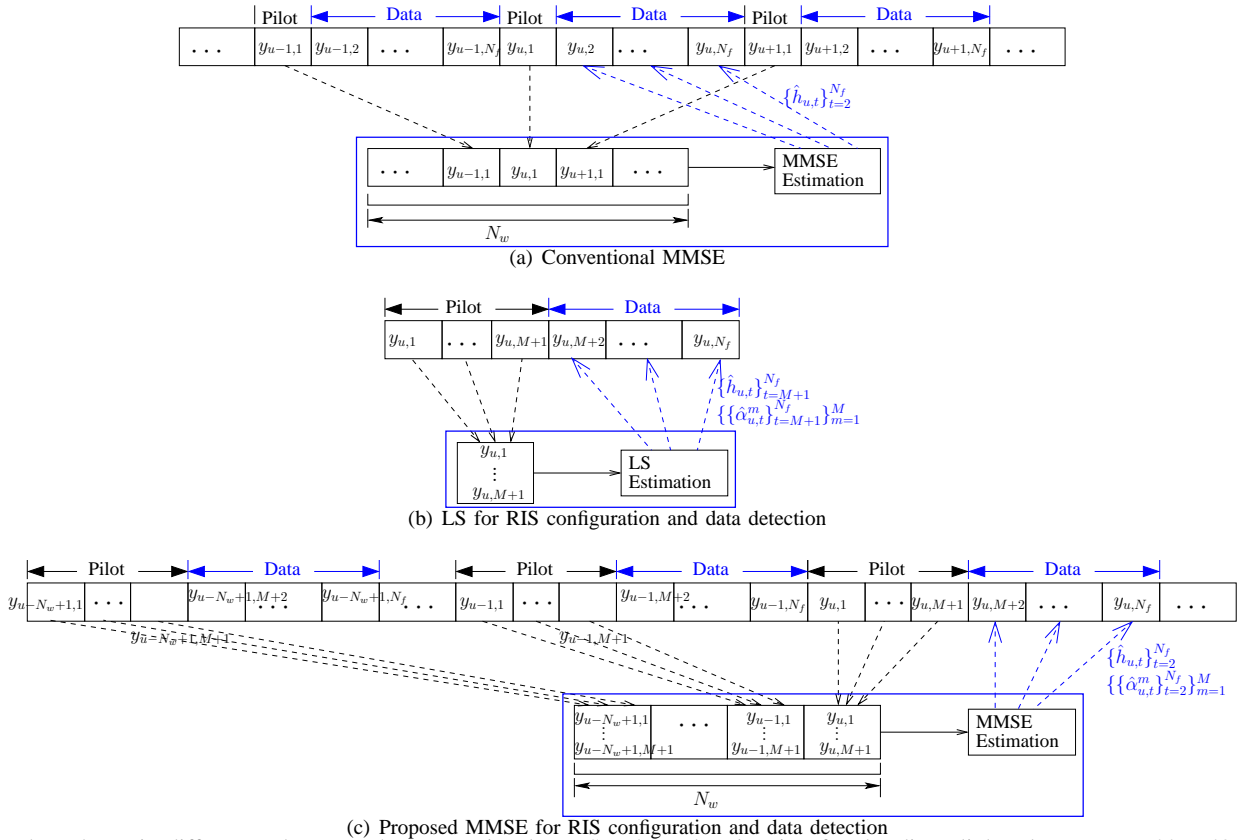


Fig. 3: The schematic differences between the conventional MMSE channel estimation for the direct-link-only systems [44], [48], [50]–[52], the ON/OFF and DFT based LS channel estimation techniques for the stationary RIS-assisted systems [27]–[31] and the proposed ON/OFF-based MMSE for the high-mobility RIS-assisted systems.

data transmission. This control information can be conveyed by a separate link such as bluetooth, and the associated time duration has negligible impact on the data rate compared to the pilot overhead, as assumed in [27]–[31].

A. Channel Estimation Techniques for Stationary RIS-Assisted Systems

The ON/OFF-based LS technique [27], [28] switches off the RIS in the first time slot and then turns on a single element at a time during the subsequent M time slots. The received pilot symbols are given by:

$$\begin{aligned} y_{u,1} &= h_{u,1}^{\text{SD}} + v_{u,1}, \\ y_{u,1+m} &= h_{u,1+m}^{\text{SD}} + h_{u,1+m}^{\text{SRD}^m} + v_{u,1+m}, \quad m = 1, \dots, M. \end{aligned} \quad (17)$$

This method assumes that the fading elements remain constant over the entire frame of signal transmission. As a result, the

estimated CSI of the direct and of the reflected links are given by:

$$\begin{aligned} \hat{h}_{u,t}^{\text{SD}} &= y_{u,1}, \\ \hat{h}_{u,t}^{\text{SRD}^m} &= y_{u,1+m} - y_{u,1}, \quad t = M+2, \dots, N_f. \end{aligned} \quad (18)$$

It is worth noting that since the direct link is always on, it has to be subtracted from the reflected link as shown above.

Alternatively, the DFT-based LS technique [29]–[31] switches on all the direct links and reflected links during training. Once again, the fading channels are assumed to be constant, i.e. we have $\mathbf{h}_{u,t} = \mathbf{h}_u^p$ for all $t = 1, \dots, N_f$ in (10). As a result, the matrix form of (10) is:

$$\mathbf{y}_u^p = \mathbf{h}_u^p \boldsymbol{\alpha}_u^p + \mathbf{v}_u^p, \quad (19)$$

where we have $\mathbf{y}_u^p = [y_{u,1}, \dots, y_{u,M+1}] \in \mathbb{C}^{1 \times (M+1)}$, $\boldsymbol{\alpha}_u^p = [\boldsymbol{\alpha}_{u,1}, \dots, \boldsymbol{\alpha}_{u,M+1}] \in \mathbb{C}^{(M+1) \times (M+1)}$ and $\mathbf{v}_u^p = [v_{u,1}, \dots, v_{u,M+1}] \in \mathbb{C}^{1 \times (M+1)}$. Following this, the LS chan-

nel estimation is given by $\hat{\mathbf{h}}_u^p = \mathbf{y}_u^p(\boldsymbol{\alpha}_u^p)^{-1}$. The associated MSE is formulated as:

$$\begin{aligned} \sigma_{\text{MSE}}^2 &= E(\|\mathbf{h}_u^p - \mathbf{y}_u^p(\boldsymbol{\alpha}_u^p)^{-1}\|^2) = E(\|\mathbf{v}_u^p(\boldsymbol{\alpha}_u^p)^{-1}\|^2) \\ &\geq N_0 \text{tr} \left\{ [(\boldsymbol{\alpha}_u^p)^H \boldsymbol{\alpha}_u^p]^{-1} \right\}, \end{aligned} \quad (20)$$

where the equality holds when $E[(\mathbf{v}_u^p)^H \mathbf{v}_u^p] = N_0 \mathbf{I}_{M+1}$, and the minimum is reached when $\boldsymbol{\alpha}_u^p$ is orthogonal. As a result, the DFT matrix is a suitable choice for the RIS training pattern, where we have $[\boldsymbol{\alpha}_u^p]_{m,t} = \exp(-j \frac{2\pi m u}{M+1})$.

B. The Channel Estimation Technique Proposed for High-Mobility RIS-Assisted Systems

It is demonstrated in Sec. III-A that the DFT pattern that switches on all RIS elements during training achieves lower MSE in stationary scenarios. However, it is worth noting that the received signals can only be formulated in the matrix form of (19) that facilitates the DFT pattern, when the fading envelope is assumed to be constant over $(M+1)$ symbol periods. In order to take into account the time-varying fading generated by Clark's model, we opt for using the ON/OFF channel estimation pattern, where the fading elements vary from symbol to symbol.

First of all, in the first time slot of all frames, the RIS is switched off and the pilot symbols are utilized for estimating the direct SD link. As a result, by observing the fading correlation function over time, the SD link of any of the t -th ($t = 1, \dots, N_f$) symbol in the u -th frame can be estimated by the MMSE interpolation filter as:

$$\hat{h}_{u,t}^{\text{SD}} = \sum_{\bar{u}=u-N_w+1}^u w_{\bar{u},t}^{\text{SD}} y_{\bar{u},1} = (\mathbf{w}_{u,t}^{\text{SD}})^T \mathbf{y}_u^{\text{SD}}, \quad (21)$$

where the MMSE filter's weights are $\mathbf{w}_{u,t}^{\text{SD}} \in \mathbb{C}^{N_w \times 1}$, while the filter input vector is $\mathbf{y}_u^{\text{SD}} \in \mathbb{C}^{N_w \times 1}$ and we have $[\mathbf{y}_u^{\text{SD}}]_i = y_{u-N_w+i,1} = h_{u-N_w+i,1}^{\text{SD}} + v_{u-N_w+i,1}$. We note that the estimate $\hat{h}_{u,t}^{\text{SD}}$ is obtained from MMSE interpolation, where the filter weights $\mathbf{w}_{u,t}^{\text{SD}}$ are different for each symbol in each frame. As a result, the associated MSE is given by:

$$\begin{aligned} \sigma_{\text{MSE-SD}_{u,t}}^2 &= E(|h_{u,t}^{\text{SD}} - \hat{h}_{u,t}^{\text{SD}}|^2) \\ &= E[(h_{u,t}^{\text{SD}} - (\mathbf{w}_{u,t}^{\text{SD}})^T \mathbf{y}_u^{\text{SD}})(h_{u,t}^{\text{SD}} - (\mathbf{w}_{u,t}^{\text{SD}})^T \mathbf{y}_u^{\text{SD}})^*] \\ &= \Gamma_u^{\text{SD}} - 2(\mathbf{w}_{u,t}^{\text{SD}})^T \mathbf{e}_{u,t}^{\text{SD}} + (\mathbf{w}_{u,t}^{\text{SD}})^T \mathbf{C}_u^{\text{SD}} (\mathbf{w}_{u,t}^{\text{SD}})^*. \end{aligned} \quad (22)$$

Based on the SD channel modelling of Sec. II-B, the correlation on h_n^{SD} is given by:

$$\begin{aligned} R_{hh}^{\text{SD}} &= E[h_n^{\text{SD}}(h_n^{\text{SD}})^*] \\ &= E[(h_{n'}^{\text{SD-LoS}} + h_{n'}^{\text{SD-NLoS}})(h_n^{\text{SD-LoS}} + h_n^{\text{SD-NLoS}})^*] \\ &= \frac{\sqrt{\Gamma_n^{\text{SD}} \Gamma_{n'}^{\text{SD}} K^{\text{SD}}}}{1+K^{\text{SD}}} \exp[j2\pi(n' \Delta f_n^{\text{SD-LoS}} - n \Delta f_n^{\text{SD-LoS}})] \\ &\quad + \frac{\sqrt{\Gamma_n^{\text{SD}} \Gamma_{n'}^{\text{SD}}}}{1+K^{\text{SD}}} J_0(2\pi f_d^{\text{SD}} |n - n'|). \end{aligned} \quad (23)$$

As a result, the covariance vector in (22) is given by $\mathbf{e}_{u,t}^{\text{SD}} = \mathbf{R}_{yh}^{\text{SD}} = E[\mathbf{y}_u^{\text{SD}}(h_{u,t}^{\text{SD}})^*]$, where $[\mathbf{e}_{u,t}^{\text{SD}}]_i = R_{hh}^{\text{SD}}$ is associated with $n' = (u - N_w + i)N_f + 1$ and $n = uN_f + t$. Furthermore, the auto-correlation matrix in (22) is given by $\mathbf{C}_u^{\text{SD}} = \mathbf{R}_{yy}^{\text{SD}} = E[\mathbf{y}_u^{\text{SD}}(\mathbf{y}_u^{\text{SD}})^H]$, where $[\mathbf{C}_u^{\text{SD}}]_{i,j} = R_{hh}^{\text{SD}}$ for $i \neq j$ and $[\mathbf{C}_u^{\text{SD}}]_{i,i} = R_{hh}^{\text{SD}} + N_0$, where R_{hh}^{SD} is associated with

$n' = (u - N_w + i)N_f + 1$ and $n = (u - N_w + j)N_f + 1$. Finally, $\frac{\partial \sigma_{\text{MSE-SD}_{u,t}}^2}{\partial (\mathbf{w}_{u,t}^{\text{SD}})^T} = 0$ leads to the MMSE solution of:

$$(\mathbf{w}_{u,t}^{\text{SD}})^* = (\mathbf{C}_u^{\text{SD}})^{-1} \mathbf{e}_{u,t}^{\text{SD}}. \quad (24)$$

As a result, the MSE of (22) becomes:

$$\sigma_{\text{MSE-SD}_{u,t}}^2 = \Gamma_{u,t}^{\text{SD}} - (\mathbf{e}_{u,t}^{\text{SD}})^H (\mathbf{C}_u^{\text{SD}})^{-1} \mathbf{e}_{u,t}^{\text{SD}}. \quad (25)$$

It was demonstrated in [66], [67] that the MSE lower bound of pilot-sequence-based channel estimation is given by the Cramer-Rao bound (CRB). More explicitly, the pilot-sequence-based channel estimator utilizes N_w repeated pilot samples at the beginning of each frame and the fading channels are assumed to be constant over the entire frame of signal transmission. The MSE of this estimation problem is lower-bounded by $E(|h - \hat{h}|^2) = 1/F(h)$, where h refers to the fading element, while the Fisher information function defined in [66], [67] is given by $F(h) = -E\left\{\frac{\partial^2 p(y|h)}{\partial h^2}\right\}$. The PDF $p(y|h)$ is the direct-link-only probability function based on $y = h + v$, where $v \sim \mathcal{CN}(0, N_0)$. Therefore, the CRB of the pilot-sequence-based channel estimation is given by $\text{CRB} = N_0/N_w$, which decreases as the SNR and/or the pilot sequence length is increased. However, this bound cannot be directly applied to time-varying fading channels, because the estimated fading element and the pilot are not located at the same position, as shown by (21). Nonetheless, the lower bound of (25) may still be valid for the case of block fading, in which case the covariance $\mathbf{e}_{u,t}^{\text{SD}}$ becomes a vector of ones multiplied by $\Gamma_u^{\text{SD}} = \Gamma_{u,t}^{\text{SD}}$, and the auto-correlation matrix \mathbf{C}_u^{SD} has $(\Gamma_u^{\text{SD}} + N_0)$ on its diagonal and Γ_u^{SD} as its off-diagonal elements. As a result, the MSE of (25) is lower-bounded by [52]:

$$\sigma_{\text{MSE-SD}_u}^2 \geq \Gamma_u^{\text{SD}} - \frac{N_w (\Gamma_u^{\text{SD}})^2}{N_0 + N_w \Gamma_u^{\text{SD}}} = \frac{1}{\frac{1}{\Gamma_u^{\text{SD}}} + \frac{N_w}{N_0}}. \quad (26)$$

The minimum is achieved when $f_d^{\text{SD}} = 0$ for the stationary scenario, where we have $R_{hh}^{\text{SD}} = \Gamma_u^{\text{SD}}$. This once again confirms that as either the SNR or N_w increases, the CSI estimate becomes more accurate. Furthermore, during the second to $(1+M)$ -th time slots of each frame, the RIS switches on its passive elements one by one in order to sample the reflected links. As a result, the m -th cascaded SRD link ($m = 1, \dots, M$) of the t -th symbol ($t = 2, \dots, N_f$) in the u -th frame is estimated by:

$$\hat{h}_{u,t}^{\text{SRD}_m} = \sum_{\bar{u}=u-N_w+1}^u w_{\bar{u},t}^{\text{SRD}_m} y_{\bar{u},1+m} = (\mathbf{w}_{u,t}^{\text{SRD}_m})^T \mathbf{y}_u^{\text{SRD}_m}, \quad (27)$$

where the MMSE filter weights are $\mathbf{w}_{u,t}^{\text{SRD}_m} \in \mathbb{C}^{N_w \times 1}$, while the MMSE filter input vector is given by $\mathbf{y}_u^{\text{SRD}_m} \in \mathbb{C}^{N_w \times 1}$. Since the direct SD link is always on, the previous estimate of the SD link has to be subtracted from the pilots as:

$$\begin{aligned} [\mathbf{y}_u^{\text{SRD}_m}]_i &= \hat{y}_{u-N_w+i,1+m} = y_{u-N_w+i,1+m} - \hat{h}_{u-N_w+i,1+m}^{\text{SD}} \\ &= h_{u-N_w+i,1+m}^{\text{SRD}_m} + \Delta h_{u-N_w+i,1+m}^{\text{SD}} + v_{u-N_w+i,1+m}, \end{aligned} \quad (28)$$

where the received pilot symbol is $y_{u-N_w+i,1+m} = h_{u-N_w+i,1+m}^{\text{SD}} + h_{u-N_w+i,1+m}^{\text{SRD}_m} + v_{u-N_w+i,1+m}$. Therefore, the remaining estimation error is $\Delta h_{u-N_w+i,1+m}^{\text{SD}} =$

$h_{u-N_w+i,1+m}^{\text{SD}} - \hat{h}_{u-N_w+i,1+m}^{\text{SD}}$, and the associated MSE is given by:

$$\begin{aligned} \sigma_{\text{MSE-SRD}}^2 &= E(|h_{u,t}^{\text{SRD}m} - \hat{h}_{u,t}^{\text{SRD}m}|^2) \\ &= E[(h_{u,t}^{\text{SRD}m} - (\mathbf{w}_{u,t}^{\text{SRD}m})^T \mathbf{y}_{u,t}^{\text{SRD}m})(h_{u,t}^{\text{SRD}m} - (\mathbf{w}_{u,t}^{\text{SRD}m})^T \mathbf{y}_{u,t}^{\text{SRD}m})^*] \\ &= \Gamma_{u,t}^{\text{SR}} \Gamma_{u,t}^{\text{RD}} - 2(\mathbf{w}_{u,t}^{\text{SRD}m})^T \mathbf{e}_{u,t}^{\text{SRD}m} + (\mathbf{w}_{u,t}^{\text{SRD}m})^T \mathbf{C}_u^{\text{SRD}m} (\mathbf{w}_{u,t}^{\text{SRD}m})^* \end{aligned} \quad (29)$$

Based on the SR and RD channel modelling of Secs. II-C and II-D, the correlation of $h_n^{\text{SRD}m} = (h_n^{\text{SR-LoS}} + h_n^{\text{SR-NLoS}})(h_n^{\text{RD-LoS}} + h_n^{\text{RD-NLoS}})$ is given by:

$$\begin{aligned} R_{hh}^{\text{SRD}n} &= E[h_{n'}^{\text{SRD}m} (h_{n'}^{\text{SRD}m})^*] = h_{n'}^{\text{SR-LoS}m} h_{n'}^{\text{RD-LoS}m} (h_{n'}^{\text{SR-LoS}m} h_{n'}^{\text{RD-LoS}m})^* \\ &+ h_{n'}^{\text{SR-LoS}m} (h_{n'}^{\text{SR-LoS}m})^* \frac{\sqrt{\Gamma_{n'}^{\text{RD}} \Gamma_{n'}^{\text{RD}}}}{1 + K^{\text{RD}}} J_0(2\pi f_d^{\text{RD}} |n - n'|) \\ &+ h_{n'}^{\text{RD-LoS}m} (h_{n'}^{\text{RD-LoS}m})^* \frac{\sqrt{\Gamma_{n'}^{\text{SR}} \Gamma_{n'}^{\text{SR}}}}{1 + K^{\text{SR}}} J_0(2\pi f_d^{\text{SR}} |n - n'|) \\ &+ \frac{\sqrt{\Gamma_{n'}^{\text{SR}} \Gamma_{n'}^{\text{SR}}} \sqrt{\Gamma_{n'}^{\text{RD}} \Gamma_{n'}^{\text{RD}}}}{1 + K^{\text{SR}}} J_0(2\pi f_d^{\text{SR}} |n - n'|) J_0(2\pi f_d^{\text{RD}} |n - n'|). \end{aligned} \quad (30)$$

As a result, the covariance vector is given by $\mathbf{R}_{yh}^{\text{SRD}m} = E[\mathbf{y}_u^{\text{SRD}m} (h_{u,t}^{\text{SRD}m})^*] = \mathbf{e}_{u,t}^{\text{SRD}m}$, where $[\mathbf{e}_{u,t}^{\text{SRD}m}]_i = R_{hh}^{\text{SRD}m}$ associated with $n' = (u - N_w + i)N_f + 1 + m$ and $n = uN_f + t$. Furthermore, the auto-correlation matrix is given by $\mathbf{R}_{yy}^{\text{SRD}m} = E[\mathbf{y}_u^{\text{SRD}m} (\mathbf{y}_u^{\text{SRD}m})^H] = \mathbf{C}_u^{\text{SRD}m}$ where $[\mathbf{C}_u^{\text{SRD}m}]_{i,j} = R_{hh}^{\text{SRD}m}$ for $i \neq j$ and $[\mathbf{C}_u^{\text{SRD}m}]_{i,i} = R_{hh}^{\text{SRD}m} + \sigma_{\text{MSE-SD}_{u-N_w+i,1+m}}^2 + N_0$, where $R_{hh}^{\text{SRD}m}$ is associated with $n' = (u - N_w + i)N_f + 1 + m$ and $n = (u - N_w + j)N_f + 1 + m$. Finally, $\frac{\partial \sigma_{\text{MSE-SRD}_{u,t}}^2}{\partial (\mathbf{w}_{u,t}^{\text{SRD}m})^T} = 0$ leads to the MMSE solution of:

$$(\mathbf{w}_{u,t}^{\text{SRD}m})^* = (\mathbf{C}_u^{\text{SRD}m})^{-1} \mathbf{e}_{u,t}^{\text{SRD}m}. \quad (31)$$

The resultant MSE is given by:

$$\begin{aligned} \sigma_{\text{MSE-SRD}_{u,t}}^2 &= \Gamma_{u,t}^{\text{SR}} \Gamma_{u,t}^{\text{RD}} - (\mathbf{e}_{u,t}^{\text{SRD}m})^H (\mathbf{C}_u^{\text{SRD}m})^{-1} \mathbf{e}_{u,t}^{\text{SRD}m} \\ &\geq \frac{\Gamma_{u,t}^{\text{SR}} \Gamma_{u,t}^{\text{RD}} (N_0 + \sigma_{\text{MSE-SD}_{u,t}}^2)}{N_0 + \sigma_{\text{MSE-SD}_{u,t}}^2 + \Gamma_{u,t}^{\text{SR}} \Gamma_{u,t}^{\text{RD}} N_w} = \frac{1}{\frac{1}{\Gamma_{u,t}^{\text{SR}} \Gamma_{u,t}^{\text{RD}}} + \frac{N_w}{N_0 + \sigma_{\text{MSE-SD}_{u,t}}^2}}, \end{aligned} \quad (32)$$

which is derived following the same steps as (26). The minimum is achieved, when we have $f_d^{\text{SR}} = f_d^{\text{RD}} = 0$ for the stationary scenario, where the autocorrelation $R_{hh}^{\text{SRD}n} = \Gamma_{u,t}^{\text{SR}} \Gamma_{u,t}^{\text{RD}} = \Gamma_{u,t}^{\text{SR}} \Gamma_{u,t}^{\text{RD}}$ is constant over $(t = 1, \dots, N_f)$.

Remark 1 (MSE in low-SNR and high-SNR regions): On one hand, as long as $N_0 \gg \Gamma_{u,t}^{\text{SR}} N_w$ is valid in the low-SNR region, the MSE of (26) becomes equivalent to the constant of $\Gamma_{u,t}^{\text{SR}}$, which does not improve with the SNR. Similarly, the condition of $N_0 + \sigma_{\text{MSE-SD}_{u,t}}^2 \gg \Gamma_{u,t}^{\text{SR}} \Gamma_{u,t}^{\text{RD}} N_w$ in the low-SNR region leads to the constant of $\Gamma_{u,t}^{\text{SR}} \Gamma_{u,t}^{\text{RD}}$ for (32). Therefore, the proposed MMSE solution cannot guarantee a better MSE than that of the DFT-based channel estimation of (20) in the low-SNR region. On the other hand, when N_0 is reduced to a value smaller than $\Gamma_{u,t}^{\text{SR}} N_w$ in the high-SNR region, the increased $\frac{N_w}{N_0}$ of (26) and $\frac{N_w}{N_0 + \sigma_{\text{MSE-SD}_{u,t}}^2}$ of (32) lead to a monotonically decreasing MSE with N_0 . By contrast, both the ON/OFF-based and DFT-based LS techniques designed for the stationary RIS assisted systems of Sec. III-A suffer from an error floor in high-mobility scenarios, which will be confirmed by our simulation results of Sec. IV.

Remark 2 (Implementations for ON/OFF RIS configuration): We note that in practice, the ON/OFF RIS configuration used for channel estimation may be facilitated by the recent

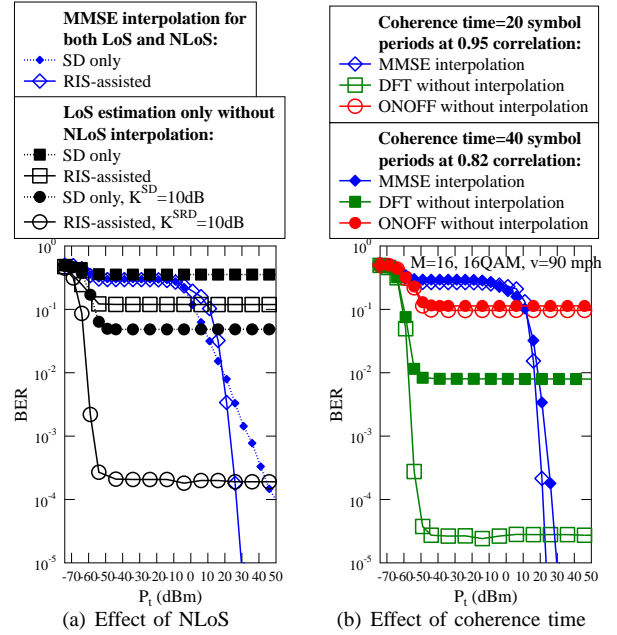


Fig. 4: BER performance results for the justification of the proposed MMSE interpolation, where the effect of NLoS and the effect of the time-varying fading even within coherence time are portrayed.

developments of simultaneous reflection and absorption aided metasurfaces [68]. DOCOMO has recently announced the successful trial of transparent metasurfaces, which are capable of achieving the dynamic manipulation of both reflection and penetration of radio waves [69]. Specifically, the positive-intrinsic-negative (PIN) diodes can be switched between "ON" and "OFF" states by controlling its biasing voltage [4]–[6].

IV. PERFORMANCE RESULTS

A. Simulation Parameters

The key parameters used for the terrestrial vehicular scenario of Fig. 1(a) are summarized in Table III, where the normalized Doppler frequencies are given by $f_d^{\text{SR}} = f_d^{\text{RD}} = \frac{v f_c}{c f_s}$ and $f_d^{\text{SR}} = 0$. The destination's coordinate is instantaneously updated by $x_D = 290 - \frac{v n}{f_s}$ from the initial coordinates of Table III over a frame length of $N_f = \lfloor (M + 1)/\eta_p \rfloor$. A total number of at least 10^3 frames are transmitted, which guarantee at least 100 bit-errors for evaluating the BER results in our simulations. The receiver noise power density is assumed to be -174 dBm/Hz. The transmit power P_t in dBm is evaluated by adding the required SNR to the noise power of $-174 + 50 = -124$ dBm. The conclusions in this section are all drawn based on the relative performance difference between the conventional direct-link-only MMSE channel estimation [44], [48], [50]–[52] as well as the ON/OFF and DFT based LS channel estimation techniques conceived for stationary RIS-assisted systems [27]–[31] and finally, the proposed ON/OFF-based MMSE solution for high-mobility RIS-assisted systems. Our simulation codes can be found at [70].

B. Justification of MMSE Interpolation

Fig. 4 demonstrates the justification of the proposed MMSE interpolation for RIS channel estimation. On one hand, the RIS assisted system models of [71]–[73] only take into account

TABLE III: Summary of parameters.

Initial coordinates	$(x_S, y_S, z_S) = (0, 0, 0)$, $(x_R, y_R, z_R) = (300, 10, 0)$, $(x_D, y_D, z_D) = (290, -10, 0)$
Path loss factors	$\gamma^{\text{SD}} = 3.8$, $\gamma^{\text{SR}} = \gamma^{\text{SD}} = 2.0$, $\text{PL}_0 = 30$ dB
Ricean K-factors	$K^{\text{SD}} = -6$ dB, $K^{\text{SR}} = 0$ dB, $K^{\text{SD}} = 0$ dB
Normalized maximum Doppler	$f_d^{\text{SD}} = f_d^{\text{RD}} = \frac{v f_c}{c f_s}$, $f_d^{\text{SR}} = 0$
Carrier frequency	2.6GHz (S-band)
Bandwidth	100 kHz
Receiver noise power density	-174 dBm/Hz

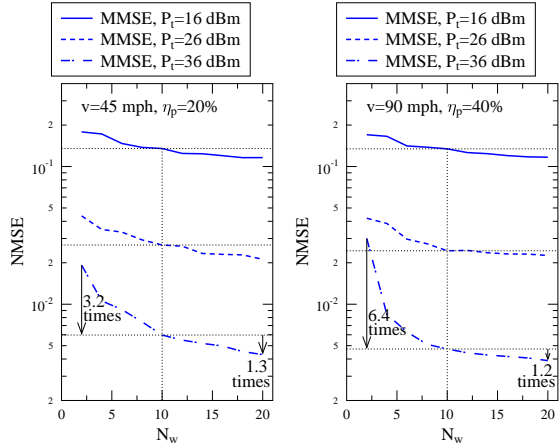
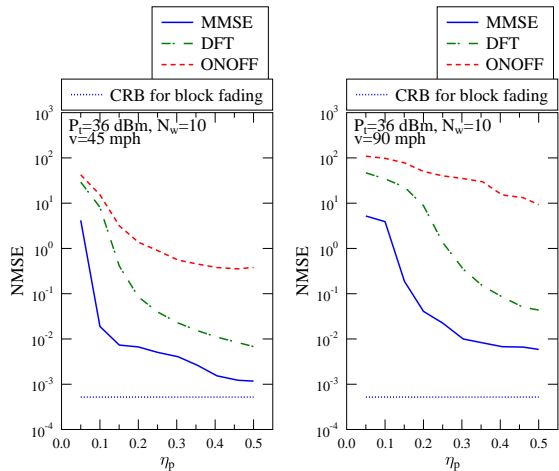
(a) Effect of N_w , $v = 45$ mph (b) Effect of N_w , $v = 90$ mph(c) Effect of η_p , $v = 45$ mph (d) Effect of η_p , $v = 90$ mph

Fig. 5: NMSE comparison between the ON/OFF and DFT based LS channel estimation techniques for stationary RIS-assisted systems [27]–[31] and the proposed ON/OFF-based MMSE solution for high-mobility RIS-assisted systems, where $M = 16$ is used.

the LoS paths, which result in irreducible error floor in the presence of NLoS paths even at high values of $K^{\text{SD}} = K^{\text{SRD}} = 10$ dB, as demonstrated by Fig. 4(a). On the other hand, the DFT and ON/OFF based methods of [27]–[31], [74] assume block fading within the coherence time, which also results in irreducible error floors, when realistic time-varying fading is taken into account, as demonstrated by Fig. 4(b). By contrast, the proposed MMSE interpolation used for RIS channel estimation is capable of mitigating the error floors, while achieving increased rates in high-mobility systems, which will be further demonstrated in the following sections.

C. Normalized MSE on Channel Estimation

In Figs. 6 and 7, generally a higher pilot percentage η_p is used, when the number of RIS elements M is increased. This is due to the fact that the channel estimation patterns

require $(1 + M)$ time slots for pilot transmission, which takes up a higher percentage as M increases. Nonetheless, the frame length N_f is adjustable, where a longer N_f leads to a higher pilot separation across frames. This degrades the CSI estimation accuracy, especially when the velocity is increased. More explicitly, the number of MMSE filter taps N_w and the pilot percentage η_p are investigated in Fig. 5 in terms of the NMSE of $\bar{\sigma}_{\text{NMSE}}^2 = E(\|\mathbf{h}_{u,t} - \hat{\mathbf{h}}_{u,t}\|^2 / \|\mathbf{h}_{u,t}\|^2)$. More explicitly, Figs. 5(a) and (b) demonstrate that as expected, the NMSE generally decreases as N_w increases. Moreover, it can also be observed in Figs. 5(a) and (b) that for both cases of $v = 45$ mph and $v = 90$ mph, the NMSE reduction achieved by increasing N_w beyond ($N_w = 10$) becomes substantially smaller than that achieved by increasing N_w from ($N_w = 2$) to ($N_w = 10$). Therefore, the choice of ($N_w = 10$) is assumed in the rest of this paper. Furthermore, Figs. 5(c) and (d) confirm once again that the proposed MMSE solution has the most accurate CSI estimate in terms of its NMSE, followed by the conventional DFT-based LS and by the ON/OFF-based LS techniques. Finally, we note that the MSE of RIS channel estimation is lower bounded by the CRB for the idealistic block fading scenarios of (26) and (32), which are also marked in Figs. 5(c) and (d). More explicitly, compared to the ON/OFF and DFT based LS techniques, the proposed ON/OFF-based MMSE solution inches closer to the idealistic quasi-static CRB in Fig. 5(c). As expected, the gap to the idealistic CRB becomes larger at the higher vehicular speed of $v = 90$ mph in Fig. 5(d), owing to the reduced fading correlation.

D. Achievable Rates

The comparisons of the achievable rates associated with Gaussian input distribution are portrayed in Fig. 6 according to Lemma 1 and Proposition 1. First of all, Fig. 6(a) demonstrates the effect of pilot percentage η_p , where the achievable rate degrades upon increasing η_p . It is also evidenced by Fig. 6(a) that the RIS assisted systems achieve higher rates than their counterparts of only using the direct SD link. Secondly, Fig. 6(b) demonstrates the effect of RIS configuration, where random RIS configuration imposes a loss on both the perfect CSI scenario of Lemma 1 and on the estimated CSI scenario of Proposition 1. The performance of using RIS random phases in the face of CSI estimation error is shown to become comparable to that of the case of only using the SD link in Fig. 6(b). We note that for the case of using RIS random phases, channel estimation is still required for data detection. The same channel estimation technique associated with the same pilot overhead is used in Fig. 6 for the sake of a fair comparison. Thirdly, Fig. 6(c) demonstrates the effect of M , where the achievable rate is improved by increasing the number of RIS elements. Finally, Fig. 6(d) demonstrates that the achievable rate also degrades as the speed of the destination

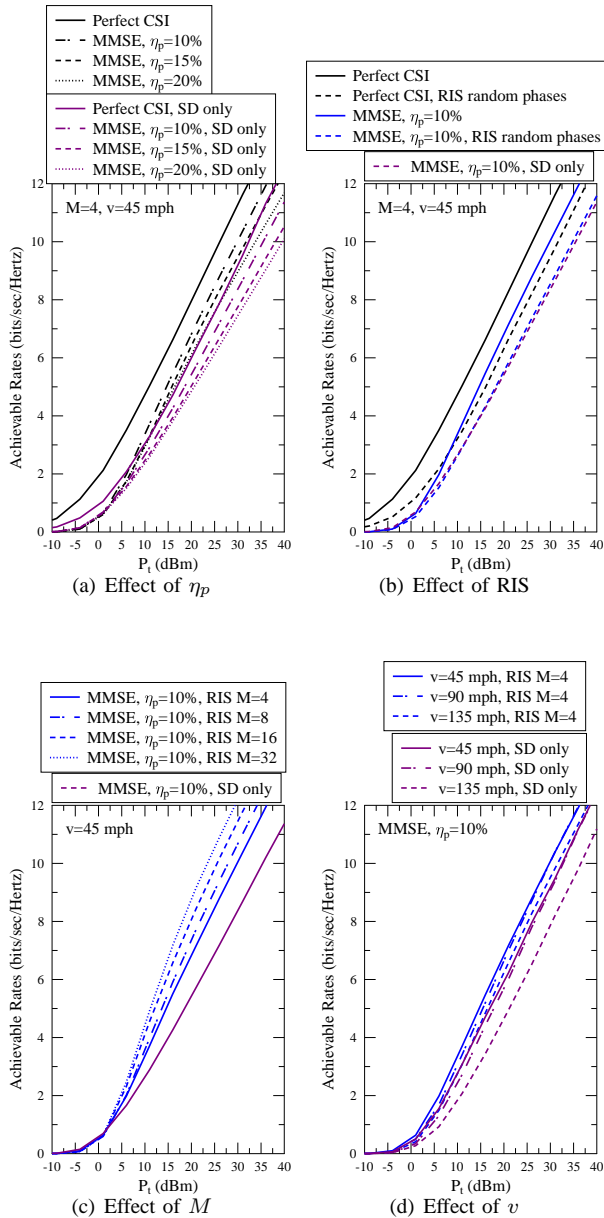


Fig. 6: The achievable rate comparison (in terms of Lemma 1 and Proposition 1 with Gaussian input) between the ON/OFF and DFT based LS channel estimation techniques for stationary RIS-assisted systems [27]–[31] and the proposed ON/OFF-based MMSE solution for high-mobility RIS-assisted systems.

node increases, where the RIS assisted systems still outperform their counterparts operating without RIS.

The comparisons of the achievable rates associated with *LPSK/QAM* input constellations are portrayed in Fig. 7 according to Lemma 2 and Proposition 2. Firstly, Fig. 7(a) portrays the relationship between Lemma 1 and Lemma 2, where the achievable rate of Lemma 2 saturates at the specific value of BPS. Fig. 7(a) also confirms that the RIS assisted systems perform better than the direct SD link operating without RIS, which is further improved as the number of RIS elements is increased from $M = 4$ to $M = 16$. Secondly, Fig. 7(b) demonstrates that when a realistic practical channel estimation technique is considered, the achievable rate of Proposition 2 peaks at $(1 - \eta_p)$ BPS, which then degrades as η_p increases. However, as the Doppler frequency increases due to the increased vehicle speed, a higher pilot percentage η_p

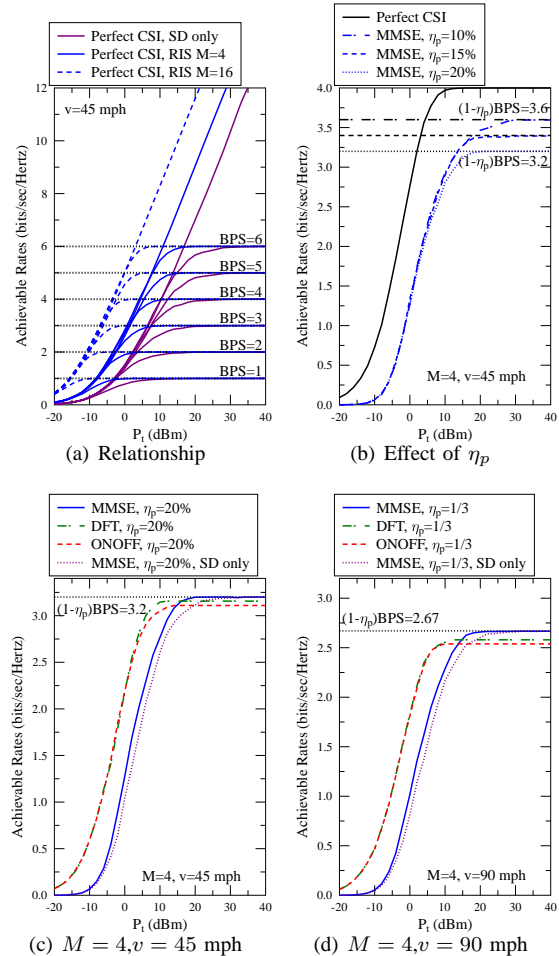


Fig. 7: The achievable rate comparison (in terms of discrete memoryless channel of Lemma 2 and Proposition 2) between the ON/OFF and DFT based LS channel estimation techniques for stationary RIS-assisted systems [27]–[31] and the proposed ON/OFF-based MMSE solution for high-mobility RIS-assisted systems.

is necessary for accurate channel estimation, which will be investigated in the next section. Finally, Figs. 7(c) and 7(d) demonstrate that the conventional ON/OFF and DFT based LS techniques conceived for stationary scenarios perform better in the low-SNR region, but they cannot achieve the full maximum rate of $(1 - \eta_p)$ BPS. This indicates that the ON/OFF and DFT based LS techniques suffer from irreducible error floors in high-mobility scenarios, which will be confirmed by the system's BER in Sec. IV-E.

E. BER performance

The capacity results of Figs. 6 and 7 are further confirmed by the system's BER performance of Fig. 8. First of all, when perfect CSI is assumed, the RIS-assisted system is capable of achieving substantial performance gains over its direct-link-only counterpart, which are 13 dB at $\text{BER}=10^{-4}$ for the case of using ($M = 4$) and 16QAM at ($v = 45$) mph in Fig. 8(a); 18 dB at $\text{BER}=10^{-4}$ for the case of using ($M = 16$) and 16QAM at ($v = 45$) mph in Fig. 8(b); 17 dB at $\text{BER}=10^{-4}$ for the case of using ($M = 16$) and 16QAM at ($v = 90$) mph in Fig. 8(c); and 17 dB at $\text{BER}=10^{-4}$ for the case of using ($M = 16$) and 64QAM at ($v = 45$) mph in Fig. 8(d). Secondly, as expected, channel estimation becomes more challenging and substantial performance gaps

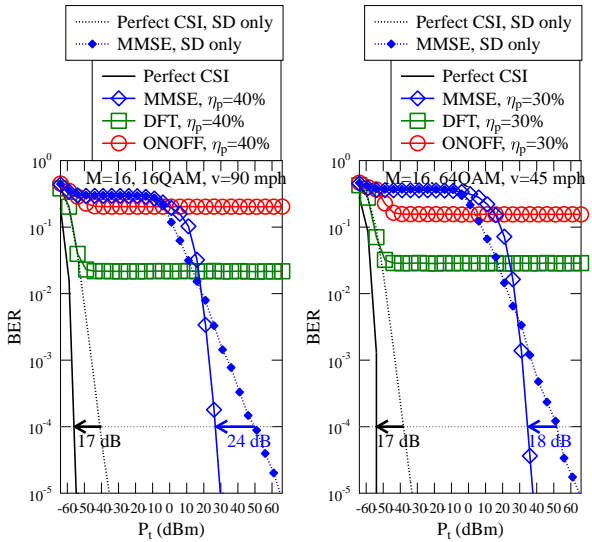
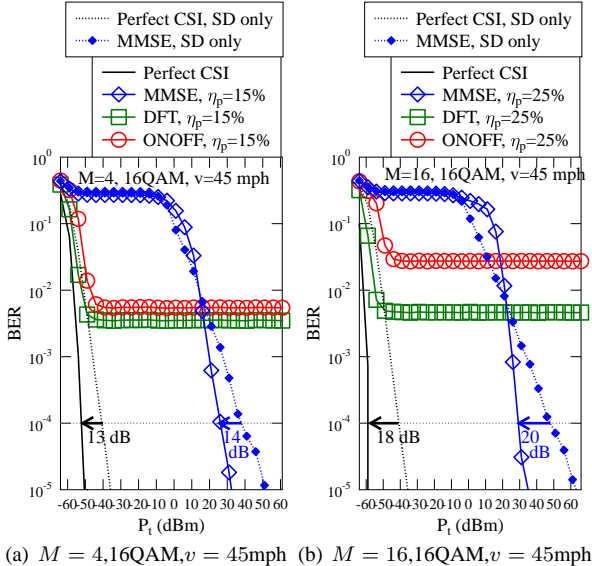


Fig. 8: BER performance comparison between the ON/OFF and DFT based LS channel estimation techniques for stationary RIS-assisted systems [27]–[31] and the proposed ON/OFF-based MMSE solution for high-mobility RIS-assisted systems, where the benchmarks of direct SD link without RIS are also portrayed.

are observed in Figs. 8(a)–(d) between the perfect CSI and estimated CSI aided direct-link-only schemes. Furthermore, as expected, the conventional ON/OFF and DFT based LS channel estimation techniques suffer from irreducible error floors in high-mobility scenarios, as evidenced by Fig. 8(a)–(d). By contrast, the proposed MMSE solution designed for the RIS-assisted arrangement is capable of achieving significant performance improvements over its direct-link-only counterpart even in high-mobility scenarios. More explicitly, the substantial performance gains achieved by the proposed MMSE scheme are represented by 14 dB at $\text{BER}=10^{-4}$ in the scenario of using ($M = 4$) and 16QAM at ($v = 45$) mph in Fig. 8(a); 20 dB at $\text{BER}=10^{-4}$ in the scenario of using ($M = 16$) and 16QAM at ($v = 45$) mph in Fig. 8(b); 24 dB at $\text{BER}=10^{-4}$ in the scenario of using ($M = 16$) and 16QAM at ($v = 90$) mph in Fig. 8(c); and 18 dB at $\text{BER}=10^{-4}$ in the scenario of using ($M = 16$) and 64QAM at ($v = 45$) mph in Fig. 8(d).

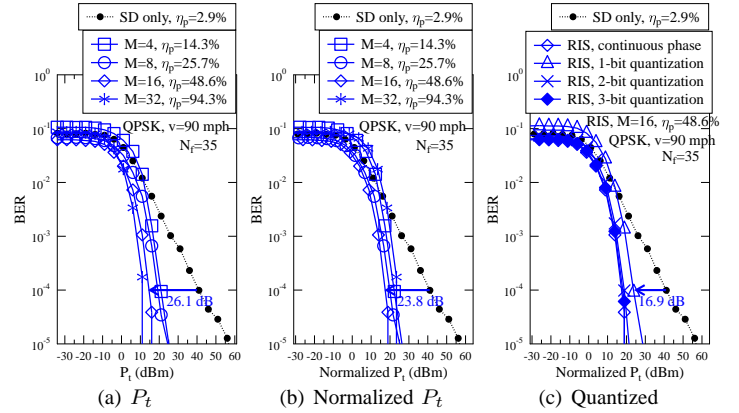


Fig. 9: BER performance of the proposed ON/OFF-based MMSE solution for high-mobility RIS-assisted systems in comparison to its counterpart of direct SD link without RIS, where QPSK is employed at $v = 40$ mph. The pilot spacing is fixed to be $N_f = 35$. The normalized transmit power is given by $P_t - 10 \log_{10}(1 - \eta_p)$ (dBm).

F. The Number of RIS Elements and RIS Quantization

The effect of M is investigated in Fig. 9. We note that the frame length N_f is also the pilot spacing. Without RIS, the pilot percentage is given by $\eta_p = \frac{1}{N_f}$. With RIS, the pilot percentage becomes $\eta_p = \frac{M+1}{N_f}$, which increases with M as seen in Fig. 9. As a result, after normalizing the transmit power by $P_t - 10 \log_{10}(1 - \eta_p)$ (dBm), the performance of using ($M = 32$) becomes even worse than using ($M = 16$) in Fig. 9(b). Nonetheless, it is confirmed by Fig. 9(b) that using a simple scheme having as few as ($M = 16$) RIS elements is sufficient to attain a substantial 23.8 dB power-efficiency gain at $\text{BER}=10^{-4}$ for a vehicle travelling at 90 mph. The motivation of deploying RIS is to compensate the path loss, where the difference of the power-efficiency gains of $26.1 - 23.8 = 2.3$ dB between Fig. 9(a) and Fig. 9(b) due to the throughput loss of ($\eta_p = 48.6\%$) for ($M = 16$) is relatively insignificant. Finally, Fig. 9(c) demonstrates that for discrete-phase RIS, 1-bit RIS quantization is sufficient for achieving a substantial power-efficiency gain of 16.9 dB at $\text{BER}=10^{-4}$, while using 2-bit quantization achieves similar performance to the case of idealistic continuous-phase RIS. In summary, for the high-mobility scenarios considered in this treatise, a small number of ($M = 16$) is sufficient for the RIS to achieve substantial gain in power-efficiency, where the RIS quantization does not impose significant impairment.

G. The Location of the Destination

Fig. 10 investigates the power-efficiency gain of using RIS, when the user is travelling to different locations. More explicitly, the transmit powers P_t (dBm) for $\text{BER}=10^{-4}$ at different user location of $(x_D, y_D, z_D) = (x_D, -10, 0)$ are recorded on the top right subfigures of Figs. 10(a) and (b), while the power-efficiency gains are recorded on the bottom right subfigures. A reference maximum transmit power of $P_t = 40$ (dBm) is indicated in Figs. 10(a) and (b), where the situation of requiring more than 40 dBm is deemed to be out of coverage.

It can be seen in Fig. 10(a) that for the case of $v = 45$ mph, the RIS achieves a higher power-efficiency gain, when the user is closer to the RIS location of $(x_R, y_R, z_R) = (300, 10, 0)$. On one hand, when the user moves closer to the BS location

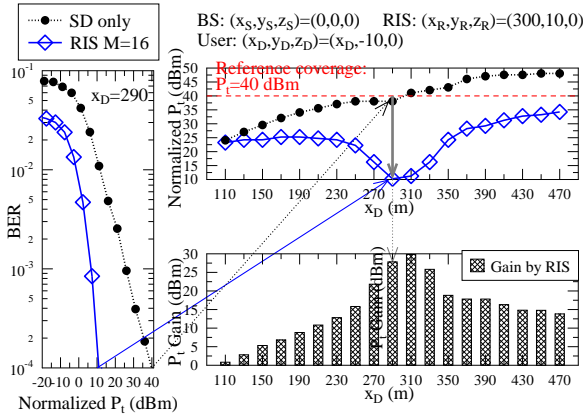
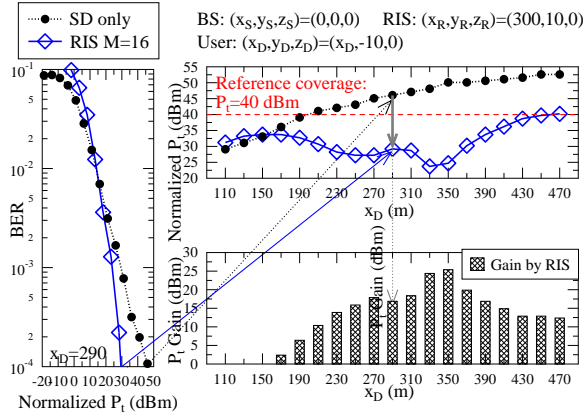
(a) $v = 45$ mph(b) $v = 90$ mph

Fig. 10: The power-efficiency gain of using RIS ($M = 16$) in terms of the required transmit power P_t (dBm) for achieving target BER of 10^{-4} , when the user is travelling to different locations of $(x_D, y_D, z_D) = (x_D, -10, 0)$. The pilot spacing is given by $N_f = 68$ and $N_f = 42$ for $v = 45$ mph and $v = 90$ mph, respectively. The transmit power is normalized by pilot percentage as $P_t - 10 \log_{10}(1 - \eta_p)$ (dBm). QPSK is used. The proposed MMSE solution is invoked for channel estimation.

of $(x_S, y_S, z_S) = (0, 0, 0)$, the direct SD link becomes strong enough so that harnessing the RIS gradually loses its advantage. On the other hand, when the user moves away from the BS beyond $(x_D = 300)$ m, the case of using only the direct SD link becomes out of coverage. However, by using RIS associated with $(M = 16)$ elements, the proposed MMSE solution is capable of reducing the required P_t below the coverage limit for a wider range of user locations up to $(x_D = 470)$ m.

Compared to Fig. 10(a), the RIS is shown to be even more critical for the increased $v = 90$ mph in Fig. 10(b). More explicitly, due to the increased mobility, the user using only direct SD link become out of coverage for $x_D > 190$ m, but the RIS is capable of assisting in extending the coverage to a wider range of up to $(x_D = 430)$ m, as evidenced by Fig. 10(b).

Once again, we note that the error floors observed in Fig. 8 imply that the conventional RIS channel estimation techniques conceived for block fading [27]–[31] cannot achieve the target BER in time-varying fading channels, regardless of how high P_t is.

H. The Path Loss Exponent

In the previous sections, the PL exponent γ^{SD} is set to be higher than those of the reflected links, as summarized

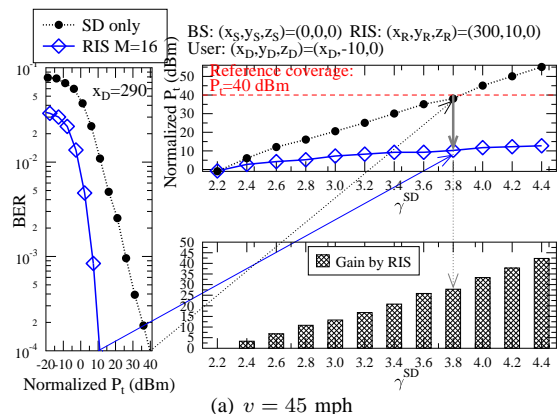
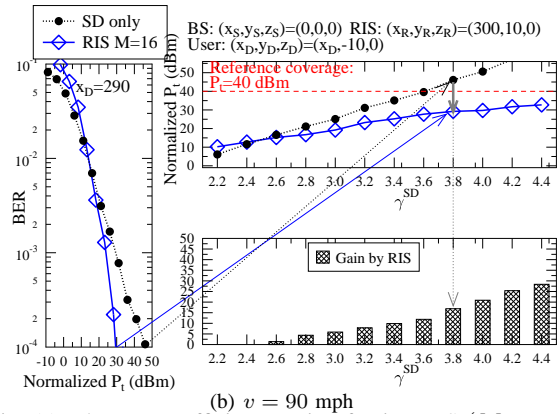
(a) $v = 45$ mph(b) $v = 90$ mph

Fig. 11: The power-efficiency gain of using RIS ($M = 16$) in terms of the required transmit power P_t (dBm) for achieving target BER of 10^{-4} , for a range of different PL exponent of the SD link γ^{SD} . The coordinates are fixed as given in Table III. The pilot spacing is given by $N_f = 68$ and $N_f = 42$ for $v = 45$ mph and $v = 90$ mph, respectively. QPSK is used. The transmit power is normalized by pilot percentage as $P_t - 10 \log_{10}(1 - \eta_p)$ (dBm).

in Table III, where the direct SD link assumes severe path loss, blockage and high NLoS attenuation. Fig. 11 further investigates the performance of the RIS assisted high-mobility systems for a range of different γ^{SD} . For the case of $v = 45$ mph, Fig. 11(a) demonstrates that the proposed MMSE solution for RIS is capable of achieving substantial power-efficiency improvements that grow with γ^{SD} for a wide range of $\gamma^{SD} > 2.2$, especially when the case of only using the direct SD link exceeds the reference coverage at $\gamma^{SD} > 3.8$. Compared to Fig. 11(a), the power-efficiency gains seen in Fig. 11(b) become smaller due to the increased $v = 90$ mph. However, Fig. 11(b) once again demonstrates that the deployment of RIS becomes more critical at the high mobility of $v = 90$ mph, where the direct SD link becomes out of coverage at $\gamma^{SD} > 3.6$, but the RIS is shown to be capable of assisting in extending the coverage over a wide range of $2.4 < \gamma^{SD} \leq 4.4$.

V. CONCLUSIONS

In this work, we propose a novel channel estimation technique for RIS-assisted high-mobility communication systems, which is capable of producing accurate CSI estimates for the sake of both RIS configuration and data detection. The analytical and numerical results confirm the advantage of the proposed technique. Our simulation results demonstrate that the proposed MMSE solution designed for RIS assisted high-

mobility systems is capable of achieving substantial power-efficiency gains for a wide range of different parameters including user moving speed, modulation level, the number of RIS elements, the user location and the path loss exponent.

APPENDIX A PROOF OF LEMMA 1

Firstly, owing to the fact that $h_{u,t}^{\text{SR}^m} \in \mathcal{CN}(\sqrt{\frac{\Gamma^{\text{SR}} K^{\text{SR}}}{1+K^{\text{SR}}}}, \frac{\Gamma^{\text{SR}}}{1+K^{\text{SR}}})$ and $h_{u,t}^{\text{RD}^m} \in \mathcal{CN}(\sqrt{\frac{\Gamma^{\text{RD}} K^{\text{RD}}}{1+K^{\text{RD}}}}, \frac{\Gamma^{\text{RD}}}{1+K^{\text{RD}}})$ are independent ergodic complex Gaussian processes, their product $h_{u,t}^{\text{SRD}^m} = h_{u,t}^{\text{SR}^m} h_{u,t}^{\text{RD}^m}$ is non-Gaussian but still ergodic [75, p42] with the mean of $\sqrt{\frac{\Gamma^{\text{SR}} \Gamma^{\text{RD}} K^{\text{SR}} K^{\text{RD}}}{(1+K^{\text{SR}})(1+K^{\text{RD}})}}$ and the variance of $\Gamma^{\text{SR}} \Gamma^{\text{RD}} - \frac{\Gamma^{\text{SR}} \Gamma^{\text{RD}} K^{\text{SR}} K^{\text{RD}}}{(1+K^{\text{SR}})(1+K^{\text{RD}})}$. Secondly, for any RIS configuration, the unitary matrix $\text{diag}(\alpha_{u,t})$ of (9) does not change the distribution of $\mathbf{h}_{u,t}^{\text{RD}} \text{diag}(\alpha_{u,t}) \mathbf{h}_{u,t}^{\text{SR}} = \sum_{m=1}^M \alpha_{u,t}^m h_{u,t}^{\text{SRD}^m}$. Therefore, the overall fading process $h_{u,t}^{\text{RIS}} = h_{u,t}^{\text{SD}} + \sum_{m=1}^M \alpha_{u,t}^m h_{u,t}^{\text{SRD}^m}$ is also ergodic, along with the following mean and variance:

$$\begin{aligned} \mu &= \sqrt{\frac{\Gamma^{\text{SD}} K^{\text{SD}}}{1+K^{\text{SD}}}} + M \sqrt{\frac{\Gamma^{\text{SR}} \Gamma^{\text{RD}} K^{\text{SR}} K^{\text{RD}}}{(1+K^{\text{SR}})(1+K^{\text{RD}})}} \\ \sigma^2 &= \frac{\Gamma^{\text{SD}}}{1+K^{\text{SD}}} + M \left[\Gamma^{\text{SR}} \Gamma^{\text{RD}} - \frac{\Gamma^{\text{SR}} \Gamma^{\text{RD}} K^{\text{SR}} K^{\text{RD}}}{(1+K^{\text{SR}})(1+K^{\text{RD}})} \right]. \end{aligned} \quad (33)$$

Based on the central limit theorem, the overall fading process $h_{u,t}^{\text{RIS}}$ becomes *Gaussian* as M becomes large, hence (11) becomes the ergodic capacity of a Ricean fading channel, where the input distribution of $s_{u,t}$ is Gaussian. Furthermore, based on (10), the received SNR is a function of $\{\alpha_{u,t}^m\}_{m=1}^M$ yielding:

$$\frac{|h_{u,t}^{\text{SD}} + \sum_{m=1}^M \alpha_{u,t}^m h_{u,t}^{\text{SRD}^m}|^2}{N_0} = \frac{|h_{u,t}^{\text{SD}}|^2 |\sum_{m=0}^M \beta_{u,t}^m \exp(j\Omega_{u,t}^m)|^2}{N_0}, \quad (34)$$

where we have $\beta_{u,t}^0 = 1$, $\{\beta_{u,t}^m = |h_{u,t}^{\text{SRD}^m}|/|h_{u,t}^{\text{SD}}|\}_{m=1}^M$, $\Omega_{u,t}^0 = 0$ and $\{\Omega_{u,t}^m = \angle \alpha_{u,t}^m + \angle h_{u,t}^{\text{SRD}^m} - \angle h_{u,t}^{\text{SD}}\}_{m=1}^M$. Considering that $|\sum_{m=0}^M \beta_{u,t}^m \exp(j\Omega_{u,t}^m)|^2 = \sum_{m=0}^M |\beta_{u,t}^m|^2 + 2 \sum_{m=0}^M \sum_{m'=m+1}^M \beta_{u,t}^m \beta_{u,t}^{m'} \cos(\Omega_{u,t}^m - \Omega_{u,t}^{m'})$, (34) is maximized when $\{\Omega_{u,t}^m = \Omega_{u,t}^0\}_{m=1}^M$, the optimum RIS configuration is thus given by $\angle \alpha_{u,t}^m = \angle h_{u,t}^{\text{SD}} - \angle h_{u,t}^{\text{SRD}^m}$, or equivalently $\alpha_{u,t}^m = \frac{h_{u,t}^{\text{SD}} (h_{u,t}^{\text{SRD}^m})^*}{|h_{u,t}^{\text{SD}} h_{u,t}^{\text{SRD}^m}|}$. The overall fading process with optimized RIS is given by $h_{u,t}^{\text{RIS}} = h_{u,t}^{\text{SD}} \left(1 + \frac{\sum_{m=1}^M |h_{u,t}^{\text{SRD}^m}|}{|h_{u,t}^{\text{SD}}|} \right)$, which leads to (11b).

APPENDIX B PROOF OF PROPOSITION 1

Firstly, since $\hat{h}_{u,t}^{\text{SD}}$ is an MMSE estimate of $h_{u,t}^{\text{SD}}$, the CSI estimation error $\Delta h_{u,t}^{\text{SD}}$ is Gaussian-distributed with zero mean and is independent of $\hat{h}_{u,t}^{\text{SD}}$ [76], i.e. we have $E(h_{u,t}^{\text{SD}} | \hat{h}_{u,t}^{\text{SD}}) = \hat{h}_{u,t}^{\text{SD}}$ and $E(|\Delta h_{u,t}^{\text{SD}}|^2 | \hat{h}_{u,t}^{\text{SD}}) = E(|\Delta h_{u,t}^{\text{SD}}|^2)$. Similarly, for the MMSE estimates of the RIS-reflected links, we have $E(h_{u,t}^{\text{SRD}^m} | \hat{h}_{u,t}^{\text{SRD}^m}) = \hat{h}_{u,t}^{\text{SRD}^m}$ and $E(|\Delta h_{u,t}^{\text{SRD}^m}|^2 | \hat{h}_{u,t}^{\text{SRD}^m}) = E(|\Delta h_{u,t}^{\text{SRD}^m}|^2)$. Moreover, the RIS now configured by $\hat{\alpha}_{u,t}^m = \frac{\hat{h}_{u,t}^{\text{SD}} (\hat{h}_{u,t}^{\text{SRD}^m})^*}{|\hat{h}_{u,t}^{\text{SD}} \hat{h}_{u,t}^{\text{SRD}^m}|}$. Therefore, the overall fading process is given by $h_{u,t}^{\text{RIS}} = h_{u,t}^{\text{SD}} + \sum_{m=1}^M \hat{\alpha}_{u,t}^m h_{u,t}^{\text{SRD}^m}$ and the CSI estimation error is given by $\Delta h_{u,t}^{\text{RIS}} = h_{u,t}^{\text{RIS}} - \hat{h}_{u,t}^{\text{RIS}} = \Delta h_{u,t}^{\text{SD}} + \sum_{m=1}^M \hat{\alpha}_{u,t}^m \Delta h_{u,t}^{\text{SRD}^m}$.

Since the RIS phases $\hat{\alpha}_{u,t}^m$ do not change the distributions of $\Delta h_{u,t}^{\text{SRD}^m}$ (see proof for Lemma 1), the sum of Gaussian distributed CSI errors leads to the Gaussian distribution for $\Delta h_{u,t}^{\text{RIS}}$, where we have $E(h_{u,t}^{\text{RIS}} | \hat{h}_{u,t}^{\text{RIS}}) = \hat{h}_{u,t}^{\text{RIS}}$ and $E(|\Delta h_{u,t}^{\text{RIS}}|^2 | \hat{h}_{u,t}^{\text{RIS}}) = E(|\Delta h_{u,t}^{\text{RIS}}|^2)$. Therefore, Corollary 3.0.2 of [76] can be invoked for the RIS-assisted system model of (10). Explicitly, it was proved in [76] that the achievable rate in terms of the generalized mutual information of using the Gaussian input distribution for the random variable $s_{u,t}$ and detection based on the MMSE CSI of $\hat{h}_{u,t}^{\text{RIS}}$ for the fading process of $h_{u,t}^{\text{RIS}}$ is given by $E \left\{ \log_2 \left[1 + \frac{|\hat{h}_{u,t}^{\text{RIS}}|^2}{N_0 + E(|\Delta h_{u,t}^{\text{RIS}} - \hat{h}_{u,t}^{\text{RIS}}|^2)} \right] \right\}$, leading to (13a). Furthermore, (13b) is given by replacing $\hat{\alpha}_{u,t}^m$ of (13b) by $\hat{\alpha}_{u,t}^m = \frac{\hat{h}_{u,t}^{\text{SD}} (\hat{h}_{u,t}^{\text{SRD}^m})^*}{|\hat{h}_{u,t}^{\text{SD}} \hat{h}_{u,t}^{\text{SRD}^m}|}$.

REFERENCES

- [1] M. D. Renzo, M. Debbah, D. T. Phan-Huy, A. Zappone, M. S. Alouini, C. Yuen, V. Sciancalepore, G. C. Alexandropoulos, J. Hoydis, H. Gacanin, and J. D. Rosny, "Smart radio environments empowered by reconfigurable AI meta-surfaces: An idea whose time has come," *EURASIP J. Wireless Commun. Netw.*, no. 1, pp. 1–20, 2019.
- [2] E. Basar, M. Di Renzo, J. De Rosny, M. Debbah, M. Alouini, and R. Zhang, "Wireless communications through reconfigurable intelligent surfaces," *IEEE Access*, vol. 7, pp. 116753–116773, 2019.
- [3] Q. Wu and R. Zhang, "Intelligent reflecting surface enhanced wireless network via joint active and passive beamforming," *IEEE Trans. Wireless Commun.*, vol. 18, no. 11, pp. 5394–5409, 2019.
- [4] Q. Wu and R. Zhang, "Towards smart and reconfigurable environment: Intelligent reflecting surface aided wireless network," *IEEE Commun. Mag.*, vol. 58, no. 1, pp. 106–112, 2020.
- [5] L. Dai, B. Wang, M. Wang, X. Yang, J. Tan, S. Bi, S. Xu, F. Yang, Z. Chen, M. D. Renzo, C. Chae, and L. Hanzo, "Reconfigurable intelligent surface-based wireless communications: Antenna design, prototyping, and experimental results," *IEEE Access*, vol. 8, pp. 45913–45923, 2020.
- [6] S. Gong, X. Lu, D. T. Hoang, D. Niyato, L. Shu, D. I. Kim, and Y. Liang, "Towards smart wireless communications via intelligent reflecting surfaces: A contemporary survey," *IEEE Commun. Surveys Tut.*, 2020.
- [7] T. J. Cui, M. Q. Qi, X. Wan, J. Zhao, and Q. Cheng, "Enabling large intelligent surfaces with compressive sensing and deep learning," *Light: Science & Applications*, vol. 3, no. 10, p. 218, 2014.
- [8] J. N. Laneman, D. N. C. Tse, and G. W. Wornell, "Cooperative diversity in wireless networks: Efficient protocols and outage behavior," *IEEE Trans. Inf. Theory*, vol. 50, no. 12, pp. 3062–3080, 2004.
- [9] G. Farhadi and N. C. Beaulieu, "On the ergodic capacity of multi-hop wireless relaying systems," *IEEE Trans. Wireless Commun.*, vol. 8, no. 5, pp. 2286–2291, 2009.
- [10] L. Wang and L. Hanzo, "The resource-optimized differentially modulated hybrid af/df cooperative cellular uplink using multiple-symbol differential sphere detection," *IEEE Signal Process. Lett.*, vol. 16, no. 11, pp. 965–968, 2009.
- [11] C. Xu, S. X. Ng, and L. Hanzo, "Near-capacity irregular convolutional coded cooperative differential linear dispersion codes using multiple-symbol differential detection," *IEEE Signal Process. Lett.*, vol. 18, no. 3, pp. 173–176, 2011.
- [12] H. V. Nguyen, C. Xu, S. X. Ng, and L. Hanzo, "Non-coherent near-capacity network coding for cooperative multi-user communications," *IEEE Trans. Commun.*, vol. 60, no. 10, pp. 3059–3070, 2012.
- [13] C. Huang, A. Zappone, G. C. Alexandropoulos, M. Debbah, and C. Yuen, "Reconfigurable intelligent surfaces for energy efficiency in wireless communication," *IEEE Trans. Wireless Commun.*, vol. 18, no. 8, pp. 4157–4170, 2019.
- [14] B. Di, H. Zhang, L. Li, L. Song, Y. Li, and Z. Han, "Practical hybrid beamforming with finite-resolution phase shifters for reconfigurable intelligent surface based multi-user communications," *IEEE Trans. Veh. Technol.*, vol. 69, no. 4, pp. 4565–4570, 2020.
- [15] C. Pan, H. Ren, K. Wang, W. Xu, M. El-kashlan, A. Nallanathan, and L. Hanzo, "Multicell MIMO communications relying on intelligent reflecting surfaces," *IEEE Trans. Wireless Commun.*, pp. 1–1, 2020.

- [16] M. Cui, G. Zhang, and R. Zhang, "Secure wireless communication via intelligent reflecting surface," *IEEE Wireless Commun. Lett.*, vol. 8, no. 5, pp. 1410–1414, 2019.
- [17] X. Yu, D. Xu, Y. Sun, D. W. K. Ng, and R. Schober, "Robust and secure wireless communications via intelligent reflecting surfaces," *arXiv preprint arXiv:1912.01497*, 2019.
- [18] H. Sheng, C. Pan, H. Ren, K. Wang, and A. Nallanathan, "Artificial-noise-aided secure mimo wireless communications via intelligent reflecting surface," *arXiv preprint arXiv:2002.07063*, 2020.
- [19] T. Bai, C. Pan, Y. Deng, M. ElKashlan, A. Nallanathan, and L. Hanzo, "Latency minimization for intelligent reflecting surface aided mobile edge computing," *IEEE J. Sel. Areas Commun.*, pp. 1–1, 2020.
- [20] C. Pan, H. Ren, K. Wang, M. ElKashlan, A. Nallanathan, J. Wang, and L. Hanzo, "Intelligent reflecting surface aided MIMO broadcasting for simultaneous wireless information and power transfer," *IEEE J. Sel. Areas Commun.*, pp. 1–1, 2020.
- [21] Y. Han, W. Tang, S. Jin, C. Wen, and X. Ma, "Large intelligent surface-assisted wireless communication exploiting statistical CSI," *IEEE Trans. Veh. Technol.*, vol. 68, no. 8, pp. 8238–8242, 2019.
- [22] K. Ying, Z. Gao, S. Lyu, Y. Wu, H. Wang, and M. Alouini, "GMD-based hybrid beamforming for large reconfigurable intelligent surface assisted millimeter-wave massive MIMO," *IEEE Access*, vol. 8, pp. 19530–19539, 2020.
- [23] J. He, H. Wymeersch, T. Sanguanpuak, O. Silven, and M. Juntti, "Adaptive beamforming design for mmWave RIS-aided joint localization and communication," in *2020 IEEE Wireless Commun. Networking Conf. Workshops (WCNCW)*, pp. 1–6, 2020.
- [24] A. Taha, M. Alrabeiah, and A. Alkhateeb, "Enabling large intelligent surfaces with compressive sensing and deep learning," *arXiv preprint arXiv:1904.10136*.
- [25] S. Liu, Z. Gao, J. Zhang, M. D. Renzo, and M.-S. Alouini, "Deep denoising neural network assisted compressive channel estimation for mmWave intelligent reflecting surfaces," *arXiv preprint arXiv:2006.02201*.
- [26] G. C. Alexandropoulos and E. Vlachos, "A hardware architecture for reconfigurable intelligent surfaces with minimal active elements for explicit channel estimation," in *IEEE Int. Conf. Acoustics, Speech Signal Process. (ICASSP)*, pp. 9175–9179, 2020.
- [27] Y. Yang, B. Zheng, S. Zhang, and R. Zhang, "Intelligent reflecting surface meets OFDM: Protocol design and rate maximization," *IEEE Trans. Commun.*, vol. 68, no. 7, pp. 4522–4535, 2020.
- [28] Z. Wang, L. Liu, and S. Cui, "Channel estimation for intelligent reflecting surface assisted multiuser communications: Framework, algorithms, and analysis," *IEEE Trans. Wireless Commun.*, pp. 1–1, 2020.
- [29] T. L. Jensen and E. De Carvalho, "An optimal channel estimation scheme for intelligent reflecting surfaces based on a minimum variance unbiased estimator," in *IEEE Int. Conf. Acoustics, Speech Signal Process. (ICASSP)*, pp. 5000–5004, 2020.
- [30] B. Zheng and R. Zhang, "Intelligent reflecting surface-enhanced OFDM: Channel estimation and reflection optimization," *IEEE Wireless Commun. Lett.*, vol. 9, no. 4, pp. 518–522, 2020.
- [31] Q. Nadeem, H. Alwazani, A. Kammoun, A. Chaaban, M. Debbah, and M. Alouini, "Intelligent reflecting surface-assisted multi-user MISO communication: Channel estimation and beamforming design," *IEEE Open J. the Commun. Society*, vol. 1, pp. 661–680, 2020.
- [32] C. You, B. Zheng, and R. Zhang, "Channel estimation and passive beamforming for intelligent reflecting surface: Discrete phase shift and progressive refinement," *IEEE J. Sel. Areas Commun.*, 2020.
- [33] C. You, B. Zheng, and R. Zhang, "Progressive channel estimation and passive beamforming for intelligent reflecting surface with discrete phase shifts," *arXiv preprint arXiv:1912.10646*.
- [34] P. Wang, J. Fang, H. Duan, and H. Li, "Compressed channel estimation for intelligent reflecting surface-assisted millimeter wave systems," *IEEE Signal Process. Lett.*, vol. 27, pp. 905–909, 2020.
- [35] J. Chen, Y.-C. Liang, H. V. Cheng, and W. Yu, "Channel estimation for reconfigurable intelligent surface aided multi-user MIMO systems," *arXiv preprint arXiv:1912.03619*.
- [36] X. Ma, Z. Chen, W. Chen, Z. Li, Y. Chi, C. Han, and S. Li, "Joint channel estimation and data rate maximization for intelligent reflecting surface assisted terahertz MIMO communication systems," *IEEE Access*, vol. 8, pp. 99565–99581, 2020.
- [37] Z. He and X. Yuan, "Cascaded channel estimation for large intelligent metasurface assisted massive mimo," *IEEE Wireless Commun. Lett.*, vol. 9, no. 2, pp. 210–214, 2020.
- [38] S. Xia and Y. Shi, "Intelligent reflecting surface for massive device connectivity: Joint activity detection and channel estimation," in *IEEE Inter. Conf. Acoustics, Speech Signal Process. (ICASSP)*, 2020.
- [39] J. Kang, "Intelligent reflecting surface: Joint optimal training sequence and reflection pattern," *IEEE Commun. Lett.*, 2020.
- [40] H. Liu, X. Yuan, and Y. A. Zhang, "Matrix-calibration-based cascaded channel estimation for reconfigurable intelligent surface assisted multiuser MIMO," *IEEE J. Sel. Areas Commun.*, pp. 1–1, 2020.
- [41] 3GPP Technical Report 21.915, "Summary of rel-15 work items," [Online]. Available: <http://www.3gpp.org/release-15>.
- [42] J. Wu and P. Fan, "A survey on high mobility wireless communications: Challenges, opportunities and solutions," *IEEE Access*, vol. 4, pp. 450–476, 2016.
- [43] R. Molina-Masegosa and J. Gozalvez, "LTE-V for sidelink 5G V2X vehicular communications: A new 5G technology for short-range vehicle-to-everything communications," *IEEE Veh. Technol. Mag.*, vol. 12, no. 4, pp. 30–39, 2017.
- [44] C. Xu, J. Zhang, T. Bai, P. Botsinis, R. G. Maunder, R. Zhang, and L. Hanzo, "Adaptive coherent/non-coherent single/multiple-antenna aided channel coded ground-to-air aeronautical communication," *IEEE Trans. Commun.*, vol. 67, no. 2, pp. 1099–1116, 2019.
- [45] C. Xu, T. Bai, J. Zhang, R. Rajashekar, R. G. Maunder, Z. Wang, and L. Hanzo, "Adaptive coherent/non-coherent spatial modulation aided unmanned aircraft systems," *IEEE Wireless Commun.*, vol. 26, no. 4, pp. 170–177, 2019.
- [46] EUROCONTROL/FAA Future Communications Study Operational Concepts and Requirements Team, "Communications operating concept and requirements (COCR) for the future radio system," *Tech. Rep. 1.0*.
- [47] J. Liu, Y. Shi, Z. M. Fadlullah, and N. Kato, "Space-air-ground integrated network: A survey," *IEEE Commun. Surveys Tuts.*, vol. 20, no. 4, pp. 2714–2741, 2018.
- [48] C. Xu, N. Ishikawa, R. Rajashekar, S. Sugiura, R. G. Maunder, Z. Wang, L. Yang, and L. Hanzo, "Sixty years of coherent versus non-coherent tradeoffs and the road from 5G to wireless futures," *IEEE Access*, vol. 7, pp. 178246–178299, 2019.
- [49] 3GPP Technical Report 36.777, "Technical specification group radio access network; study on enhanced lte support for aerial vehicles (release 15)," [Online]. Available: http://www.3gpp.org/ftp//Specs/archive/36_series/36.777/, Jan. 2018.
- [50] D. Divsalar and M. K. Simon, "Maximum-likelihood differential detection of uncoded and trellis coded amplitude phase modulation over AWGN and fading channels-metrics and performance," *IEEE Trans. Commun.*, vol. 42, pp. 76–89, Jan. 1994.
- [51] R. Schober and W. H. Gerstacker, "Decision-feedback differential detection based on linear prediction for MDPSK signals transmitted over Ricean fading channels," *IEEE Journal on Selected Areas in Commun.*, vol. 18, pp. 391–402, Mar. 2000.
- [52] J. K. Cavers, "An analysis of pilot symbol assisted modulation for Rayleigh fading channels," *IEEE Trans. Veh. Technol.*, vol. 40, pp. 686–693, Nov. 1991.
- [53] T. Cui and C. Tellambura, "On multiple symbol detection for diagonal DUSTM over Ricean channels," *IEEE Trans. Wireless Commun.*, vol. 7, pp. 1146–1151, April 2008.
- [54] R. H. Clarke, "A statistical theory of mobile radio reception," *Bell Labs Technical Journal*, vol. 47, pp. 957–1000, 1968.
- [55] W. C. Jakes, *Microwave mobile communications*. John Wiley & Sons, 1975.
- [56] J. G. Proakis, *Digital Communications*. New York: McGraw-Hill, 1995.
- [57] A. Goldsmith, *Wireless communications*. Cambridge University Press, 2005.
- [58] L. Hanzo, O. Alamri, M. El-Hajjar, and N. Wu, *Near-Capacity Multi-Functional MIMO Systems: Sphere-Packing, Iterative Detection and Cooperation*. John Wiley & Sons, May 2009.
- [59] L. Hanzo, Y. Akhtman, L. Wang, and M. Jiang, *MIMO-OFDM for LTE, WiFi and WiMAX: Coherent versus non-coherent and cooperative turbo transceivers*. John Wiley & Sons, 2011.
- [60] O. Ozdogan, E. Bjornson, and E. G. Larsson, "Intelligent reflecting surfaces: Physics, propagation, and pathloss modeling," *IEEE Wireless Commun. Lett.*, vol. 9, no. 5, pp. 581–585, 2020.
- [61] E. Bjornson and L. Sanguinetti, "Rayleigh fading modeling and channel hardening for reconfigurable intelligent surfaces," *IEEE Wireless Commun. Lett.*, vol. 10, no. 4, pp. 830–834, 2021.
- [62] E. Bjornson, O. Ozdogan, and E. G. Larsson, "Intelligent reflecting surface versus decode-and-forward: How large surfaces are needed to beat relaying?," *IEEE Wireless Commun. Lett.*, vol. 9, no. 2, pp. 244–248, 2020.
- [63] G. Ungerboeck, "Channel coding with multilevel/phase signals," *IEEE Trans. Inf. Theory*, vol. 28, no. 1, pp. 55–67, 1982.

- [64] S. X. Ng and L. Hanzo, "On the MIMO channel capacity of multidimensional signal sets," *IEEE Trans. Veh. Technol.*, vol. 55, no. 2, pp. 528–536, 2006.
- [65] C. Xu, S. Sugiura, S. X. Ng, P. Zhang, L. Wang, and L. Hanzo, "Two decades of MIMO design tradeoffs and reduced-complexity MIMO detection in near-capacity systems," *IEEE Access*, vol. 5, pp. 18564–18632, 2017.
- [66] E. De Carvalho and D. T. M. Slock, "Cramer-Rao bounds for semi-blind, blind and training sequence based channel estimation," in *IEEE Signal Process. Workshop Signal Process. Advances Wireless Commun.*, pp. 129–132, 1997.
- [67] A. Vosoughi and A. Scaglione, "Everything you always wanted to know about training: guidelines derived using the affine precoding framework and the CRB," *IEEE Trans. Signal Process.*, vol. 54, pp. 940–954, 2006.
- [68] X. Wang, J. Ding, B. Zhang, S. An, G. Zhai, and H. Zhang, "Simultaneous realization of anomalous reflection and transmission at two frequencies using bi-functional metasurfaces," *Scientific Reports*, vol. 8, no. 1, pp. 1–8, 2018.
- [69] DOCOMO, "Docomo conducts world's first successful trial of transparent dynamic metasurface," [Online]. Available: https://www.nttdocomo.co.jp/english/info/media_center/pr/2020/0117_00.html.
- [70] "Github code. accessed: May 2021.," [Online]. Available: https://github.com/cx1g08/RIS_Ricean/.
- [71] B. Matthiesen, E. Bjornson, E. D. Carvalho, and P. Popovski, "Intelligent reflecting surface operation under predictable receiver mobility: A continuous time propagation model," *IEEE Wireless Commun. Lett.*, vol. 10, no. 2, pp. 216–220, 2021.
- [72] S. Sun and H. Yan, "Channel estimation for reconfigurable intelligent surface-assisted wireless communications considering Doppler effect," *IEEE Wireless Commun. Lett.*, vol. 10, no. 4, pp. 790–794, 2021.
- [73] W. Wu, H. Wang, W. Wang, and R. Song, "Doppler mitigation method aided by reconfigurable intelligent surfaces for high-speed channels," *IEEE Wireless Commun. Lett.*, vol. 11, no. 3, pp. 627–631, 2022.
- [74] Z. Huang, B. Zheng, and R. Zhang, "Transforming fading channel from fast to slow: Intelligent refracting surface aided high-mobility communication," *IEEE Trans. Wireless Commun.*, pp. 1–1, 2021.
- [75] H. White, *Asymptotic theory for econometricians*. Academic Press, 1984.
- [76] A. Lapidath and S. Shamai, "Fading channels: how perfect need "perfect side information" be?," *IEEE Trans. Inf. Theory*, vol. 48, no. 5, pp. 1118–1134, 2002.